Planck intermediate results. XXXIII. Signature of the magnetic field geometry of interstellar filaments in dust polarization maps

Planck Collaboration, P. Ade, N. Aghanim, M. Alves, M. Arnaud, D. Arzoumanian, J. Aumont, C. Baccigalupi, J. Banday, R. Barreiro, et al.

▶ **To cite this version:**

Planck Collaboration, P. Ade, N. Aghanim, M. Alves, M. Arnaud, et al.. Planck intermediate results. XXXIII. Signature of the magnetic field geometry of interstellar filaments in dust polarization maps. Astronomy and Astrophysics - A&A, 2016, 586, pp.A136. 10.1051/0004-6361/201425305 . hal-02022195

HAL Id: hal-02022195
https://hal.science/hal-02022195

Submitted on 19 Jan 2022

HAL is a multi-disciplinary open access archive for the deposit and dissemination of scientific research documents, whether they are published or not. The documents may come from teaching and research institutions in France or abroad, or from public or private research centers.

L'archive ouverte pluridisciplinaire **HAL**, est destinée au dépôt et à la diffusion de documents scientifiques de niveau recherche, publiés ou non, émanant des établissements d'enseignement et de recherche français ou étrangers, des laboratoires publics ou privés.

Distributed under a Creative Commons Attribution 4.0 International License

A&A 586, A136 (2016)
DOI: 10.1051/0004-6361/201425305
© ESO 2016

Astronomy & Astrophysics

Planck intermediate results

XXXIII. Signature of the magnetic field geometry of interstellar filaments in dust polarization maps

Planck Collaboration: P. A. R. Ade[80], N. Aghanim[53], M. I. R. Alves[53], M. Arnaud[67], D. Arzoumanian[53,⋆], J. Aumont[53], C. Baccigalupi[79], A. J. Banday[86,8], R. B. Barreiro[58], N. Bartolo[27,59], E. Battaner[87,88], K. Benabed[54,85], A. Benoit-Lévy[21,54,85], J.-P. Bernard[86,8], O. Berné[86], M. Bersanelli[30,45], P. Bielewicz[76,8,79], A. Bonaldi[61], L. Bonavera[58], J. R. Bond[7], J. Borrill[11,82], F. R. Bouchet[54,81], F. Boulanger[53], A. Bracco[53], C. Burigana[44,28,46], E. Calabrese[84], J.-F. Cardoso[68,1,54], A. Catalano[69,66], A. Chamballu[67,13,53], H. C. Chiang[24,6], P. R. Christensen[77,34], D. L. Clements[51], S. Colombi[54,85], L. P. L. Colombo[20,60], C. Combet[69], F. Couchot[65], B. P. Crill[60,9], A. Curto[58,5,63], F. Cuttaia[44], L. Danese[79], R. D. Davies[61], R. J. Davis[61], P. de Bernardis[29], A. de Rosa[44], G. de Zotti[41,79], J. Delabrouille[1], C. Dickinson[61], J. M. Diego[58], S. Donzelli[45], O. Doré[60,9], M. Douspis[53], A. Ducout[54,51], X. Dupac[35], F. Elsner[21,54,85], T. A. Enßlin[73], H. K. Eriksen[56], E. Falgarone[66], K. Ferrière[86,8], F. Finelli[44,46], O. Forni[86,8], M. Frailis[43], A. A. Fraisse[24], E. Franceschi[44], A. Frejsel[77], S. Galeotta[43], S. Galli[62], K. Ganga[1], T. Ghosh[53], M. Giard[86,8], Y. Giraud-Héraud[1], E. Gjerløw[56], J. González-Nuevo[17,58], K. M. Górski[60,89], A. Gregorio[31,43,49], A. Gruppuso[44], V. Guillet[53], F. K. Hansen[56], D. Hanson[74,60,7], D. L. Harrison[55,63], C. Hernández-Monteagudo[10,73], D. Herranz[58], S. R. Hildebrandt[60,9], E. Hivon[54,85], M. Hobson[5], W. A. Holmes[60], K. M. Huffenberger[22], G. Hurier[53], A. H. Jaffe[51], T. R. Jaffe[86,8], W. C. Jones[24], M. Juvela[23], R. Keskitalo[11], T. S. Kisner[71], J. Knoche[73], M. Kunz[15,53,2], H. Kurki-Suonio[23,40], G. Lagache[4,53], J.-M. Lamarre[66], A. Lasenby[5,63], C. R. Lawrence[60], R. Leonardi[35], F. Levrier[66], M. Liguori[27,59], P. B. Lilje[56], M. Linden-Vørnle[14], M. López-Caniego[35,58], P. M. Lubin[25], J. F. Macías-Pérez[69], B. Maffei[61], N. Mandolesi[44,28], A. Mangilli[53,65], M. Maris[43], P. G. Martin[7], E. Martínez-González[58], S. Masi[29], S. Matarrese[27,59,38], P. Mazzotta[32], A. Melchiorri[29,47], L. Mendes[35], A. Mennella[30,45], M. Migliaccio[55,63], S. Mitra[50,60], M.-A. Miville-Deschênes[53,7], A. Moneti[54], L. Montier[86,8], G. Morgante[44], D. Mortlock[51], D. Munshi[80], J. A. Murphy[75], P. Naselsky[77,34], F. Nati[24], P. Natoli[28,3,44], H. U. Nørgaard-Nielsen[14], F. Noviello[61], D. Novikov[72], I. Novikov[77,72], N. Oppermann[7], L. Pagano[29,47], F. Pajot[53], R. Paladini[52], D. Paoletti[44,46], F. Pasian[43], F. Perrotta[79], V. Pettorino[39], F. Piacentini[29], M. Piat[1], E. Pierpaoli[20], D. Pietrobon[60], S. Plaszczynski[65], E. Pointecouteau[86,8], G. Polenta[3,42], G. W. Pratt[67], J.-L. Puget[53], J. P. Rachen[18,73], R. Rebolo[57,12,16], M. Reinecke[73], M. Remazeilles[61,53,1], C. Renault[69], A. Renzi[33,48], S. Ricciardi[44], I. Ristorcelli[86,8], G. Rocha[60,9], C. Rosset[1], M. Rossetti[30,45], G. Roudier[1,66,60], J. A. Rubiño-Martín[57,16], B. Rusholme[52], M. Sandri[44], M. Savelainen[23,40], G. Savini[78], D. Scott[19], J. D. Soler[53], V. Stolyarov[5,83,64], D. Sutton[55,63], A.-S. Suur-Uski[23,40], J.-F. Sygnet[54], J. A. Tauber[36], L. Terenzi[37,44], L. Toffolatti[17,58,44], M. Tomasi[30,45], M. Tristram[65], M. Tucci[15], L. Valenziano[44], J. Valiviita[23,40], B. Van Tent[70], P. Vielva[58], F. Villa[44], L. A. Wade[60], B. D. Wandelt[54,85,26], D. Yvon[13], A. Zacchei[43], and A. Zonca[25]

(Affiliations can be found after the references)

Received 9 November 2014 / Accepted 12 September 2015

ABSTRACT

Planck observations at 353 GHz provide the first fully sampled maps of the polarized dust emission towards interstellar filaments and their backgrounds (i.e., the emission observed in the surroundings of the filaments). The data allow us to determine the intrinsic polarization properties of the filaments and therefore to provide insight into the structure of their magnetic field (***B***). We present the polarization maps of three nearby (several parsecs long) star-forming filaments of moderate column density ($N_{\rm H}$ about 10^{22} cm^{-2}): Musca, B211, and L1506. These three filaments are detected above the background in dust total and polarized emission. We use the spatial information to separate Stokes I, Q, and U of the filaments from those of their backgrounds, an essential step in measuring the intrinsic polarization fraction (p) and angle (ψ) of each emission component. We find that the polarization angles in the three filaments ($\psi_{\rm fil}$) are coherent along their lengths and not the same as in their backgrounds ($\psi_{\rm bg}$). The differences between $\psi_{\rm fil}$ and $\psi_{\rm bg}$ are 12° and 54° for Musca and L1506, respectively, and only 6° in the case of B211. These differences for Musca and L1506 are larger than the dispersions of ψ, both along the filaments and in their backgrounds. The observed changes of ψ are direct evidence of variations of the orientation of the plane of the sky (POS) projection of the magnetic field. As in previous studies, we find a decrease of several per cent in p with $N_{\rm H}$ from the backgrounds to the crest of the filaments. We show that the bulk of the drop in p within the filaments cannot be explained by random fluctuations of the orientation of the magnetic field because they are too small ($\sigma_\psi < 10°$). We recognize the degeneracy between the dust alignment efficiency (by, e.g., radiative torques) and the structure of the ***B***-field in causing variations in p, but we argue that the decrease in p from the backgrounds to the filaments results in part from depolarization associated with the 3D structure of the ***B***-field: both its orientation in the POS and with respect to the POS. We do not resolve the inner structure of the filaments, but at the smallest scales accessible with *Planck* (~0.2 pc), the observed changes of ψ and p hold information on the magnetic field structure within filaments. They show that both the mean field and its fluctuations in the filaments are different from those of their backgrounds, which points to a coupling between the matter and the ***B***-field in the filament formation process.

Key words. dust, extinction – ISM: magnetic fields – polarization – submillimeter: ISM

⋆ Corresponding author: D. Arzoumanian, e-mail: doris.arzoumanian@ias.u-psud.fr

1. Introduction

The interstellar medium (ISM) has been observed to be filamentary for more than three decades. Filamentary structures have been observed in extinction (e.g., Schneider & Elmegreen 1979; Myers 2009), in dust emission (e.g., Abergel et al. 1994), in H I (e.g., Joncas et al. 1992; McClure-Griffiths et al. 2006), in CO emission from diffuse molecular gas (Falgarone et al. 2001; Hily-Blant & Falgarone 2009), and dense star-forming regions (e.g., Bally et al. 1987; Cambrésy 1999). Filaments are striking features of Galactic images from the far-infrared/submm *Herschel* space observatory (André et al. 2010; Motte et al. 2010; Molinari et al. 2010). They are ubiquitous both in the diffuse ISM and in star-forming molecular clouds, and the densest ones are observed to be associated with prestellar cores (e.g., Arzoumanian et al. 2011; Palmeirim et al. 2013; Konyves et al. 2015). Their formation and dynamical evolution has become a central research topic in the field of star formation (see the review by André et al. 2014, and references therein). In particular, the role played by the magnetic field is the main unanswered question.

The importance of the Galactic magnetic field for the dynamics of molecular clouds is supported by Zeeman measurements, which show that there is rough equipartition between their magnetic, gravitational, and kinetic energies (e.g., Myers & Goodman 1988; Crutcher et al. 2004). Dust polarization observations provide an additional means to study the structure of the magnetic field. For a uniform magnetic field, the observed polarization angle is perpendicular to the component of the magnetic field on the plane of the sky (POS) in emission and parallel in extinction. The polarization fraction depends on the dust polarization properties and the grain alignment efficiency, but also on the structure of the magnetic field (Hildebrand 1983). A number of studies have investigated the relative orientation between the magnetic field and filaments in molecular clouds using starlight polarization (e.g., Goodman et al. 1990; Pereyra & Magalhães 2004; Chapman et al. 2011; Sugitani et al. 2011). Dust polarized emission from the densest regions of molecular clouds, i.e., mainly dense cores and the brightest structures in nearby molecular clouds, has been observed from the ground at sub-mm wavelengths (e.g., Ward-Thompson et al. 2000; Crutcher et al. 2004; Attard et al. 2009; Matthews et al. 2001, 2009) and more recently using balloon-borne experiments (e.g., Pascale et al. 2012; Matthews et al. 2014). However, owing to the limited sensitivity and range of angular scales probed by these observations, detection of polarization from filaments and their lower column density surroundings has not been achieved. This is a limitation because, as polarization is a pseudo-vector, the polarized emission observed towards a filament depends on the polarization properties of the background. This effect is all the more important when the contrast between the filament and its background is low.

Planck[1] has produced the first all-sky map of the polarized emission from dust at sub-mm wavelengths (Planck Collaboration I 2015). The *Planck* maps of polarization angle, ψ, and fraction, p, encode information on the magnetic field structure (Planck Collaboration Int. XIX 2015). The observations have been compared to synthetic polarized emission maps computed from simulations of anisotropic magneto-hydrodynamical turbulence assuming simply a uniform intrinsic polarization fraction of dust grains (Planck Collaboration Int. XX 2015). In these simulations, the turbulent structure of the magnetic field is able to reproduce the main statistical properties of p and ψ that are observed directly in a variety of nearby clouds, dense cores excluded (see also Falceta-Gonçalves et al. 2008, 2009). Planck Collaboration Int. XX (2015) conclude that the large scatter of p at $N_{\rm H}$ smaller than 10^{22} cm^{-2} in the observations is due mainly to fluctuations in the magnetic field orientation along the line of sight (LOS) rather than to changes in grain shape and/or the efficiency of grain alignment. They also show that the large-scale field orientation with respect to the LOS plays a major role in the quantitative analysis of these statistical properties.

The *Planck* maps of total intensity, as well as polarized intensity, display the filamentary structure of the ISM (Planck Collaboration XI 2014; Planck Collaboration Int. XIX 2015; Planck Collaboration X 2015). Planck Collaboration Int. XXXII (2016) identify interstellar filaments over the intermediate latitude sky, and present a statistical analysis of their orientation with respect to the component of the magnetic field on the POS ($\boldsymbol{B}_{\rm POS}$). In the diffuse ISM, filaments are preferentially aligned with $\boldsymbol{B}_{\rm POS}$. Towards nearby molecular clouds the relative orientation changes progressively from preferentially parallel to preferentially perpendicular from the lowest to the highest column densities (Planck Collaboration Int. XXXV 2016).

In this paper, we make use of the *Planck* polarization data to study the structure of the magnetic field within three fields comprising the archetypical examples of star-forming filaments of moderate column density: B211, L1506, and Musca. Characterizing the magnetic field structure in such filaments, and its connection with that of the surrounding cloud, is a step towards understanding the role of the magnetic field in their formation and evolution. Stellar polarization data in these fields have been reported by several authors (Goodman et al. 1990; Pereyra & Magalhães 2004; Chapman et al. 2011). With *Planck* we have now access to fully sampled maps of the dust polarized emission of both the filaments and their surrounding environment. The spatial information allow us to derive the polarization properties intrinsic to the filaments after subtracting the contribution of the surrounding background to the Stokes I, Q, and U maps. We relate the results of our data analysis to the structure of the magnetic field.

The paper is organized as follows. The *Planck* data at 353 GHz and the relations used to derive the polarization parameters from the Stokes I, Q, and U maps are presented in Sect. 2. In Sect. 3, we present the I, Q, and U maps of the three filaments and their profiles perpendicular to their crests. In Sect. 4 we quantify the variations of the polarization angle and fraction from the background to the filaments, and within the filaments. Section 5 discusses possible interpretations of the observed decrease in p from the background to the filaments. Section 6 summarizes the results of our data analysis and presents perspectives to further studies. In Appendix A, we present a two-component model that applies as a first approximation to the polarized emission from interstellar filaments and their backgrounds.

2. *Planck* observations

Planck observed the sky in nine frequency bands from 30 to 857 GHz in total intensity, and in polarization up to 353 GHz (Planck Collaboration I 2014). Here, we only use the intensity and polarization data at 353 GHz, which is

[1] *Planck* (http://www.esa.int/Planck) is a project of the European Space Agency (ESA) with instruments provided by two scientific consortia funded by ESA member states and led by Principal Investigators from France and Italy, telescope reflectors provided through a collaboration between ESA and a scientific consortium led and funded by Denmark, and additional contributions from NASA (USA).

Table 1. Observed properties of the filaments.

Filament	d [pc]	Length [pc]	Width [pc]	$R_{\rm out}$ [pc]	$N_{\rm H}^{\rm fil}$ [10^{21} cm^{-2}]	$N_{\rm H}^{\rm bg}$ [10^{21} cm^{-2}]	$M_{\rm line}$ [$M_\odot$ pc^{-1}]	PA [deg]
Musca	200	10	0.75	1	8	2.2	30	30
B211	140	2.6	0.33	0.5	17	3	47	90
L1506	140	3	0.35	0.5	7	2.3	26	55

Notes. Column 3 gives the length along the filament crest. Column 4 gives the filament full width at half maximum (FWHM) derived from a Gaussian fit to the total intensity radial profile. The values given are for the observations, i.e., without beam deconvolution. The outer radius (given in Col. 5) is defined as the radial distance from the filament crest at which its radial profile amplitude is equal to that of the background (without beam deconvolution). Columns 6 and 7 give the observed column density values at the crest of the filament ($r = 0$) and at $r = R_{\rm out}$, respectively. The latter corresponds to the mean value of the background. Column 8 gives the mass per unit length estimated from the radial column density profiles of the filaments. Column 9 gives the position angle (PA) of the segment of the filament that is used to derive the mean profile. The PA (measured positively from north to east) is the angle between the Galactic north (GN) and the tangential direction to the filament crest derived from the I map.

the highest frequency *Planck* channel with polarization capabilities and the one with best signal-to-noise ratio (S/N) for dust polarization (Planck Collaboration Int. XXII 2015). The in-flight performance of the High Frequency Instrument (HFI) is described in Planck HFI Core Team (2011) and Planck Collaboration II (2014). We use a *Planck* internal release data set (DR3, delta-DX9) at 353 GHz, presented and analysed in Planck Collaboration Int. XIX (2015), Planck Collaboration Int. XX (2015), Planck Collaboration Int. XXI (2015), and Planck Collaboration Int. XXXII (2016). We ignore the polarization of the CMB, which at 353 GHz is a negligible contribution to the sky polarization towards molecular clouds (Planck Collaboration Int. XXX 2016). The I, Q, and U maps at the resolution of 4.′8 analysed here have been constructed using the gnomonic projection of the `HEALPix`[2] (Górski et al. 2005) all-sky maps. The regions that we study in this paper are within the regions of high S/N, which are not masked in Planck Collaboration Int. XIX (2015).

Stokes I, Q, and U parameters are derived from *Planck* observations. Stokes I is the total dust intensity. The Stokes Q and U parameters are the two components of the linearly polarized dust emission resulting from LOS integration and are related as

$$Q = Ip\cos(2\psi), \quad (1)$$
$$U = Ip\sin(2\psi), \quad (2)$$
$$P = \sqrt{Q^2 + U^2}, \quad (3)$$
$$p = P/I, \quad (4)$$
$$\psi = 0.5\ \arctan(U, Q), \quad (5)$$

where P is the total polarized intensity, p is the polarization fraction (see Eq. (6)), and ψ is the polarization angle given in the IAU convention (see Planck Collaboration Int. XIX 2015). The $\arctan(U, Q)$ is used to compute $\arctan(U/Q)$ avoiding the π ambiguity. The POS magnetic field orientation (χ) is obtained by adding 90° to the polarization angle ($\chi = \psi + 90°$). In the paper we show the Stokes parameter maps as provided in the `HEALPix` convention, where the *Planck* U Stokes map is given by $U = -Ip\sin(2\psi)$. Because of the noise present in the observed Stokes parameter maps, P and p are biased positively and the errors on ψ are not Gaussian (Planck Collaboration Int. XIX 2015; Montier et al. 2015). We debias P and p according to the method proposed by Plaszczynski et al. (2014), by taking into account the full noise covariance matrix of the *Planck* data.

[2] `http://healpix.sourceforge.net`

3. The filaments as seen by *Planck*

In the following, we present the *Planck* I, Q, and U maps of three filaments in two nearby molecular clouds: the Musca filament, and the Taurus B211 and L1506 filaments. The angular resolution of *Planck* (4.′8) translates into a linear resolution of 0.2 pc and 0.3 pc at the distances of the Taurus and the Musca clouds, 140 and 200 pc respectively (Franco 1991; Schlafly et al. 2014). Table 1 summarizes the main characteristics of the three filaments. We describe each of them in the following sections.

3.1. The Musca filament

Musca is a 10 pc long filament located at a distance of 200 pc from the Sun, in the north of the Chamaeleon region (Gregorio Hetem et al. 1988; Franco 1991). The mean column density along the crest of the filament is 8×10^{21} cm^{-2} as derived from the *Planck* data (Planck Collaboration Int. XXIX 2016). The magnetic field in the neighbourhood of the Musca cloud has been traced using optical polarization measurements of background stars by Pereyra & Magalhães (2004). *Herschel* SPIRE images show *hair-like* striations of matter perpendicular to the main Musca filament and aligned with the magnetic field lines (Cox et al. 2015).

Figure 1 shows the *Planck* 353 GHz Stokes parameter maps of the Musca cloud. The filament is well detected in total intensity and polarization. To quantify the polarized intensity observed towards the filament we derive radial profiles perpendicular to its crest. The crest of the filament is traced using the `DisPerSE` algorithm (Sousbie 2011; Arzoumanian et al. 2011). Cuts perpendicular to the crest of the filament are then constructed at each pixel position along the filament crest. The profiles centred on neighbouring pixels along the filament crest, corresponding to six times the beam size ($6 \times 4.'8$), are averaged to increase the S/N. The position of each of the profiles is shown on the intensity map of Fig. 1. The mean profiles are numbered from 1 to 7, running from the south to the north of the filament. Figure 2 shows the radial profiles of the Stokes parameters where hereafter r corresponds to the radial distance from the crest of the filament. The profiles in Fig. 2 illustrate the variability of the emission along the different cuts. The presence of neighbouring structures next (in projection) to the main Musca filament, can be seen in the profiles (e.g., the bumps at $r \simeq -2$ pc correspond to the elongated structure to the east of the crest of the Musca filament).

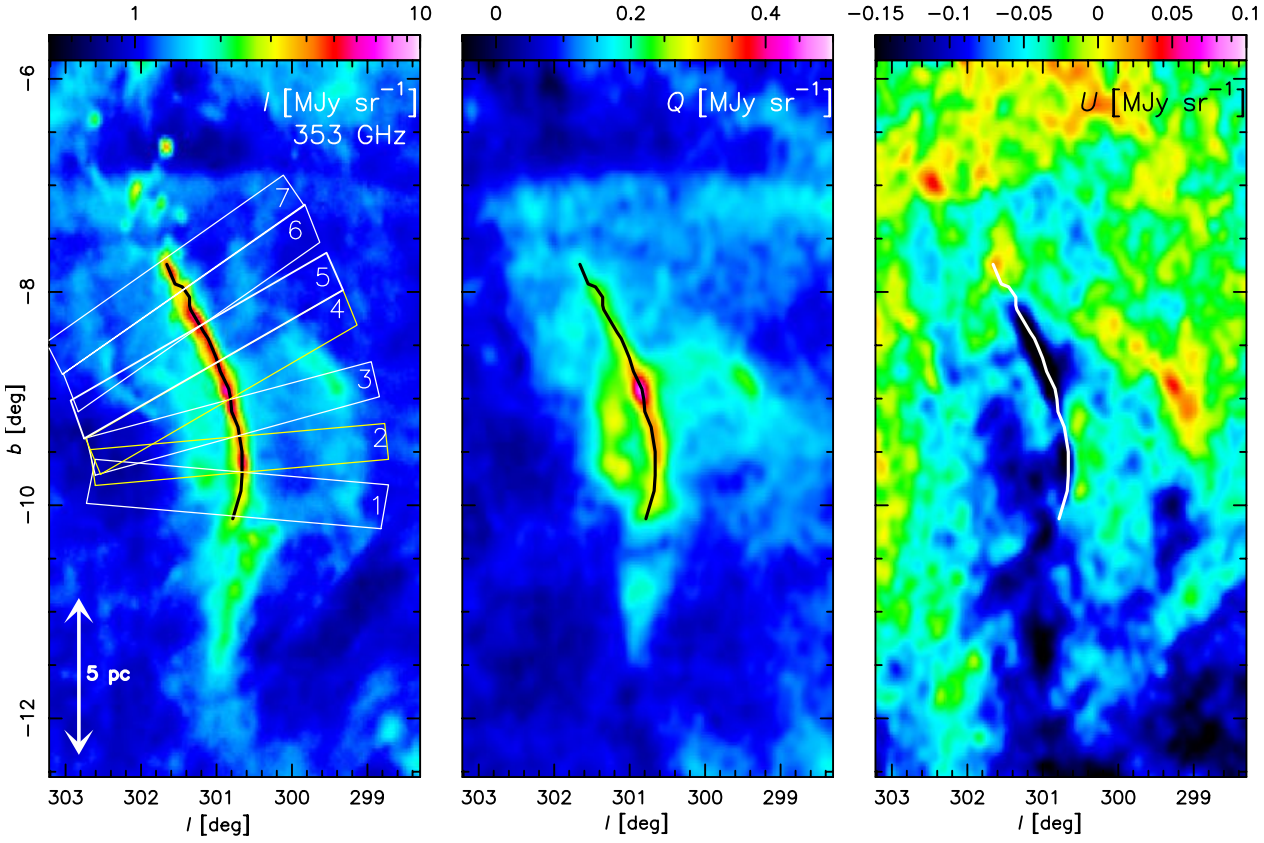

Fig. 1. *Planck* 353 GHz Stokes parameter maps of Musca (in MJy sr^{-1}). The total intensity map is at a resolution of 4.′8, while the Q and U maps are smoothed to a resolution of 9.′6 for better visualization. The crest of the filament traced on the I map is drawn in black (on the I and Q maps) and white (on the U map). The boxes drawn on the I map, numbered from 1 to 7, show the regions from which the mean profiles are derived (see Fig. 2).

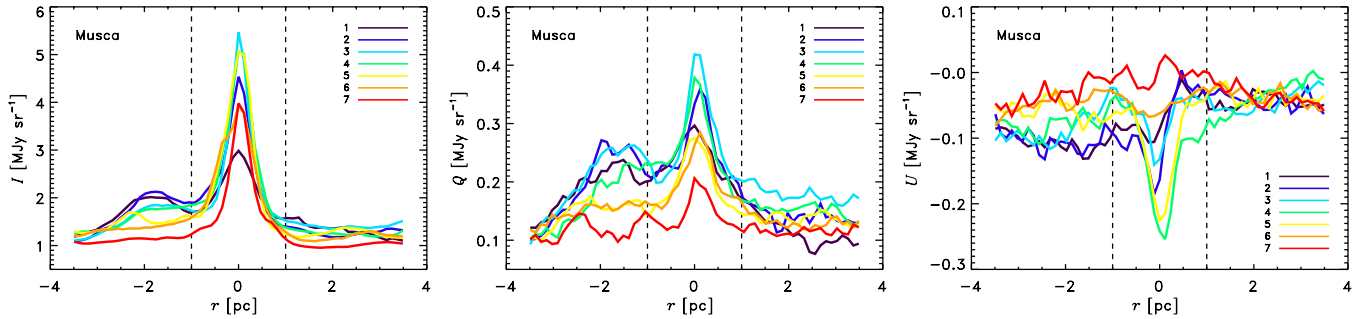

Fig. 2. Observed radial profiles perpendicular to the crest of the Musca filament. The I, Q, and U radial profiles are shown in the *left, middle, and right panels*, respectively. Values $r < 0$ correspond to the eastern side of the filament. The vertical dashed lines indicate the position of the outer radius $R_{\rm out}$. The numbers of the profiles correspond to the cuts shown on the left panel of Fig. 1.

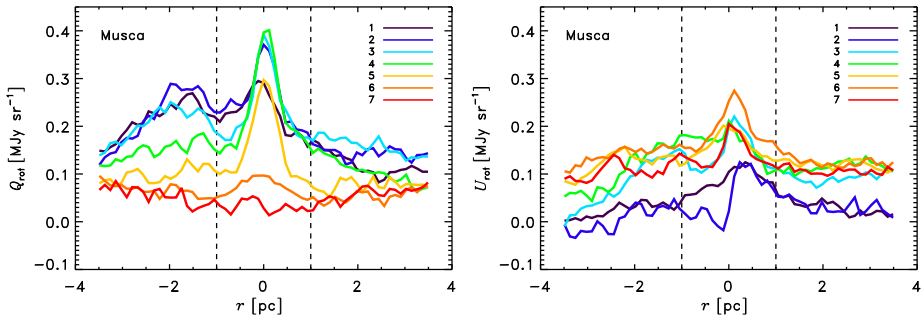

Fig. 3. Observed radial $Q_{\rm rot}$ (*left*) and $U_{\rm rot}$ (*right*) profiles of the Musca filament (same as Fig. 2) computed so that the reference direction is aligned with the filament crest.

We observe a variation of the Stokes Q and U profiles of the filament associated with the change of its orientation on the POS. Thus the observed variations in the Stokes Q and U profiles are not necessarily due to variations of the $\boldsymbol{B}$-field orientation with respect to the filament crest. In Fig. 3 the Q and U parameters, $Q_{\rm rot}$ and $U_{\rm rot}$, are computed using the filament crest as the reference direction; the position angle (PA) of each segment (1 to 7) is estimated from the mean tangential direction to the filament crest. The parameter $Q_{\rm rot}$ is positive and $U_{\rm rot} = 0$ if the magnetic field is perpendicular to the filament crest. The data (Fig. 3) show that most of the polarized emission of segments 1 to 5 is associated with $Q_{\rm rot} > 0$ and $Q_{\rm rot} > |U_{\rm rot}|$. This is consistent with a magnetic field close to perpendicular to the filament crest. For the segments 6 and 7, the relative orientation between the $\boldsymbol{B}_{\rm POS}$ angle and the filament is different as indicated by the $Q_{\rm rot}$ and $U_{\rm rot}$ profiles.

3.2. The Taurus B211 filament

The B211 filament is located in the Taurus molecular cloud (TMC). It is one of the closest star-forming regions in our Galaxy located at a distance of only 140 pc from the Sun (Elias 1978; Kenyon et al. 1994; Schlafly et al. 2014). This region has been the target of numerous observations, has long been considered as a prototypical molecular cloud of isolated low-mass star formation, and has inspired magnetically regulated models of star formation (e.g., Shu et al. 1987; Nakamura & Li 2008). The B211 filament is one of the well-studied nearby star-forming filaments that shows a number of young stars and prestellar cores along its ridge (Schmalzl et al. 2010; Li & Goldsmith 2012; Palmeirim et al. 2013). Recently, Li & Goldsmith (2012) studied the Taurus B211 filament and found that the measured densities and column densities indicate a filament width along the LOS that is equal to the width observed on the POS (~0.1 pc). Studies previous to *Planck*, using polarization observations of background stars, found that the structure of the Taurus cloud and that of the magnetic field are related (e.g., Heyer et al. 2008; Chapman et al. 2011). Using the Chandrasekhar-Fermi method, Chapman et al. (2011) estimated a magnetic field strength of about 25 μG in the cloud surrounding the B211 filament, concluding that the former is magnetically supported.

Figure 4 shows the *Planck* 353 GHz Stokes parameter maps of the TMC around the B211 and L1506 filaments. The B211 filament is well detected in the I and Q maps, as a structure distinct from its surrounding. On the U map, on the other hand, the filament is not seen as an elongated structure, but it is perpendicular to a large U gradient that separates two regions of almost uniform U. The U emission is negative on the northern side of the filament while it is positive on the southern side. This indicates that the $\boldsymbol{B}$-field orientation varies in the cloud surrounding the B211 filament. This variation can be seen very clearly in the radial profiles perpendicular to the filament crest, shown in Fig. 5. These profiles are derived as explained in the previous section (for the Musca filament). The four Q and U profiles (shown in the middle and right-hand panels of Fig. 5) are derived by averaging the cuts within a distance along the filament crest of 3 times the *Planck* beam ($3 \times 4\farcm8$). The cloud intensity (I) increases from the southern to the northern side of the filament, while the Q emission is similar on both sides of the filament crest. The (negative) Q emission of B211 is very clearly seen in the radial profiles. The different profiles show the approximate invariance of the emission along the filament crest. The total and polarized emission components are remarkably constant along the length of B211.

3.3. The Taurus L1506 filament

The L1506 filament is located on the south-east side of B211 (see Fig. 4). Stellar polarization data are presented by Goodman et al. (1990). The density structure and the dust emission properties have been studied by Stepnik et al. (2003), and more recently by Ysard et al. (2013) using *Herschel* data. This filament has mean column densities comparable to those of the Musca filament. Star formation at both ends of L1506 has been observed with the detection of a few candidate prestellar cores (Stepnik et al. 2003; Pagani et al. 2010). Figure 6 shows the radial profiles perpendicular to its crest. The colour profiles numbered from 1 to 5 (and derived as explained in Sect. 3.2), correspond to mean profiles at different positions along its crest. Profiles 1, 5, and 6 trace the emission corresponding to the star-forming cores at the two ends of the filament. The other profiles (2 to 4) trace the emission associated with the filament, not affected by emission of star-forming cores. The fluctuations seen in the Q and U profiles are of the same order as the fluctuations of the emission of B211 located a few parsecs north-west of L1506, but the polarized emission associated with the filament is much smaller (the scale of the plots in Figs. 5 and 6 is not the same). The polarized intensity observed towards L1506 is smaller than that associated with the Musca and B211 filaments, while the total intensity is of the same order of magnitude.

3.4. Polarized intensity and polarization fraction

Figure 7 presents the polarized intensity (P) maps of the two studied molecular clouds, derived from the Q and U maps using Eq. (3) and debiased according to the method proposed by Plaszczynski et al. (2014), as mentioned in Sect. 2. The POS angle of the magnetic field (χ) is overplotted on the maps; the length of the pseudo-vectors is proportional to the observed (debiased) polarization fraction. These maps show that the Musca and B211 filaments are detected in polarized emission, while the L1506 filament is not seen as an enhanced structure in polarized intensity unlike in total intensity.

The polarization fraction (p) is plotted as a function of the column density ($N_{\rm H}$) for the filaments and their backgrounds in Fig. 8. This plot shows a large scatter of p for the lowest column density values corresponding to the background in L1506 and B211 (small dots in Fig. 8). Such a scatter is present in the statistical analysis of *Planck* polarization data towards Galactic molecular clouds (see in particular Fig. 2 in Planck Collaboration Int. XX 2014). For the filaments, p decreases as a function of column density (see Fig. 8). We have drawn three lines, one for each filament. They represent the linear fit $\log p$ versus $\log N_{\rm H}$ for the data points corresponding to the filament areas with $|r| < R_{\rm out}$ and $N_{\rm H}$ larger than 2.2×10^{21}, 3×10^{21}, and 2.3×10^{21} cm^{-2} for the Musca, B211, and L1506 filaments, respectively (see Table 1). The linear dependence does not fit these data points. Only Musca shows a linear relationship that extends to the lowest column density values. The best fit slopes, $s_{p-N_{\rm H}}$, are −0.35, −0.31, and −0.23, for Musca, B211 and L1506, respectively. We point out that the specific values of $s_{p-N_{\rm H}}$ for B211 and L1506 are not well defined and depend on the separation between the data points representing the filament and the surrounding cloud. A decrease in p with $N_{\rm H}$ has been reported in previous studies and ascribed to the loss of

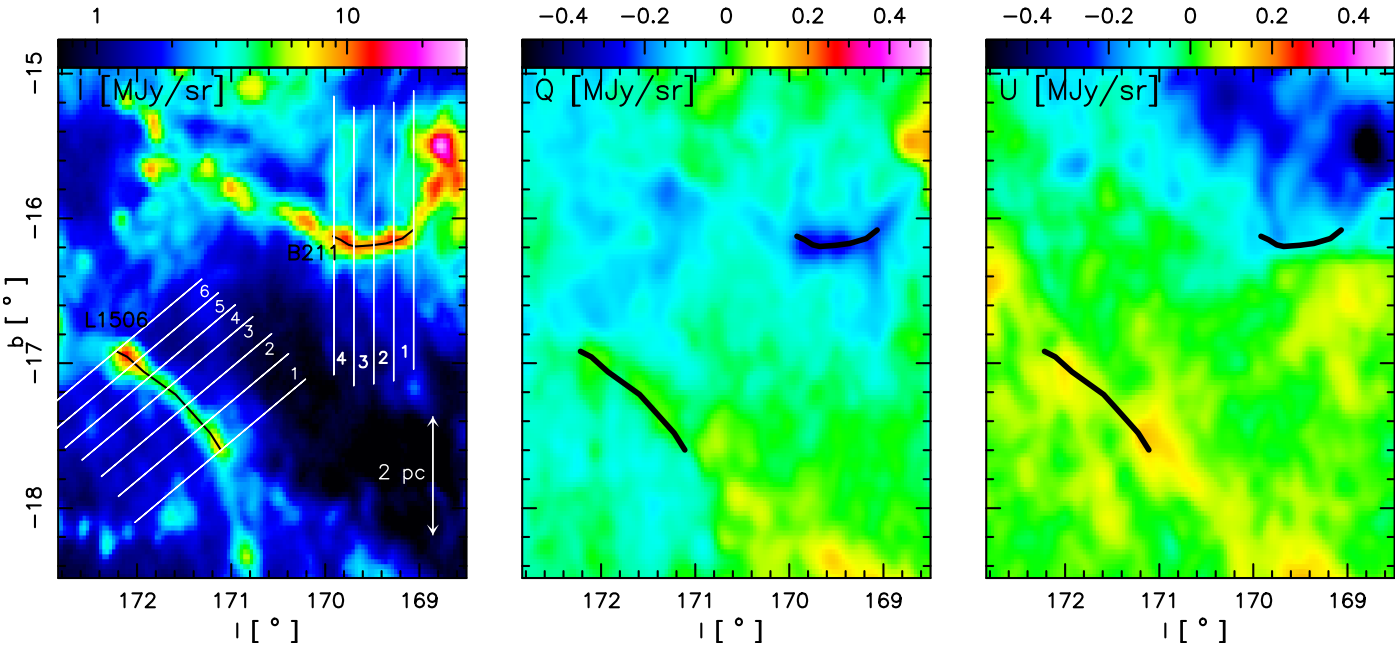

Fig. 4. Same as Fig. 1 for part of the Taurus molecular cloud around the B211 (north-west) and the L1506 (south-east) filaments. The numbers and white lines on the total intensity map correspond to the positions of the different cuts used to derive the radial profiles shown in Figs. 5 and 6.

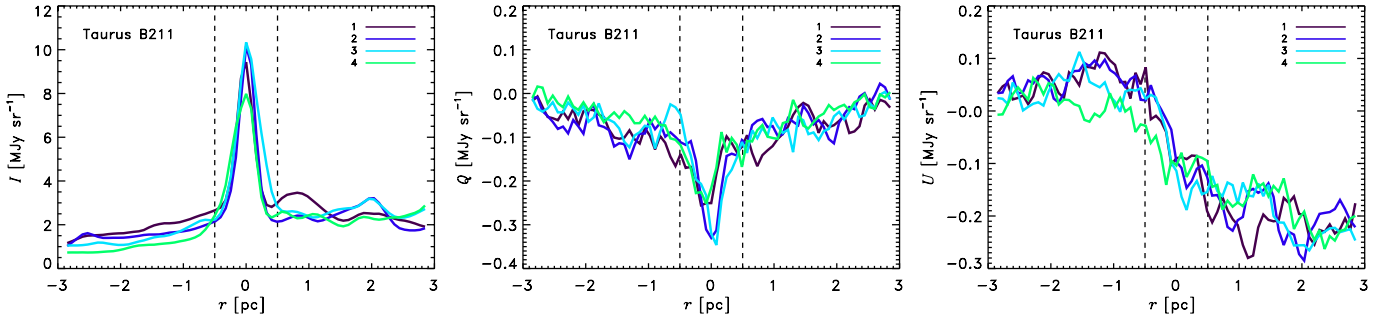

Fig. 5. Same as Fig. 2 for the Taurus B211 filament. Here $r < 0$ corresponds to the southern side of the filament crest. The filament is clearly seen in Q and is located in the area of a steep variation of the U emission. The dispersion of the emission is small along the length of the filament.

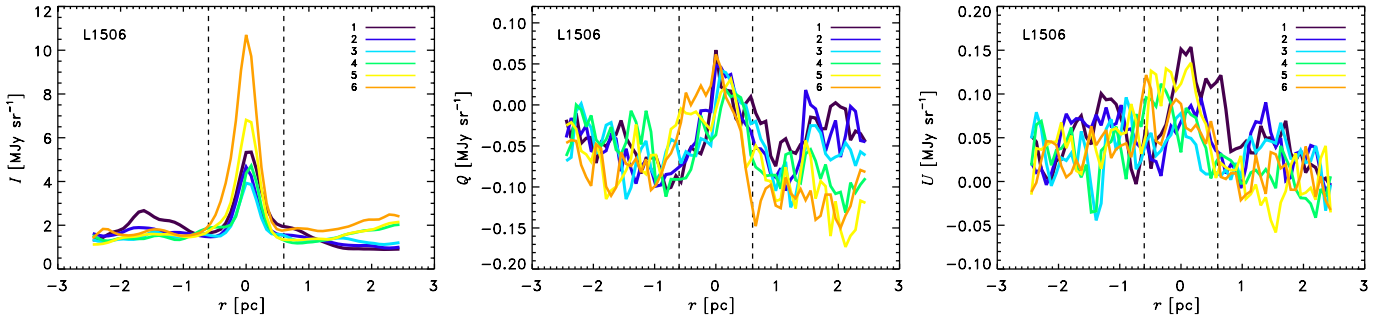

Fig. 6. Same as Fig. 2 for L1506. Here $r < 0$ corresponds to the south-eastern side of the filament crest.

grain alignment efficiency (e.g., Lazarian et al. 1997) and/or the random component of the magnetic field (e.g., Jones et al. 1992; Ostriker et al. 2001; Planck Collaboration Int. XIX 2015; Planck Collaboration Int. XX 2015). In particular Whittet et al. (2008) and Jones et al. (2015) proposed a single fit for a diverse set of data points observed towards different clouds and objects. Our analysis shows that the decrease in p with increasing $N_{\rm H}$ for all the data points is not well described by a mean power law. The p values for the filaments at a given $N_{\rm H}$ vary by more than a factor of five.

In the next sections, we take advantage of the imaging capability and sensitivity of *Planck* to further characterize the origins of the polarization properties of the filaments.

4. Polarization properties

In the following, we introduce a two-component model that uses the spatial information in *Planck* images to separate the emission of the filaments from the surrounding emission (Sect. 4.1). This

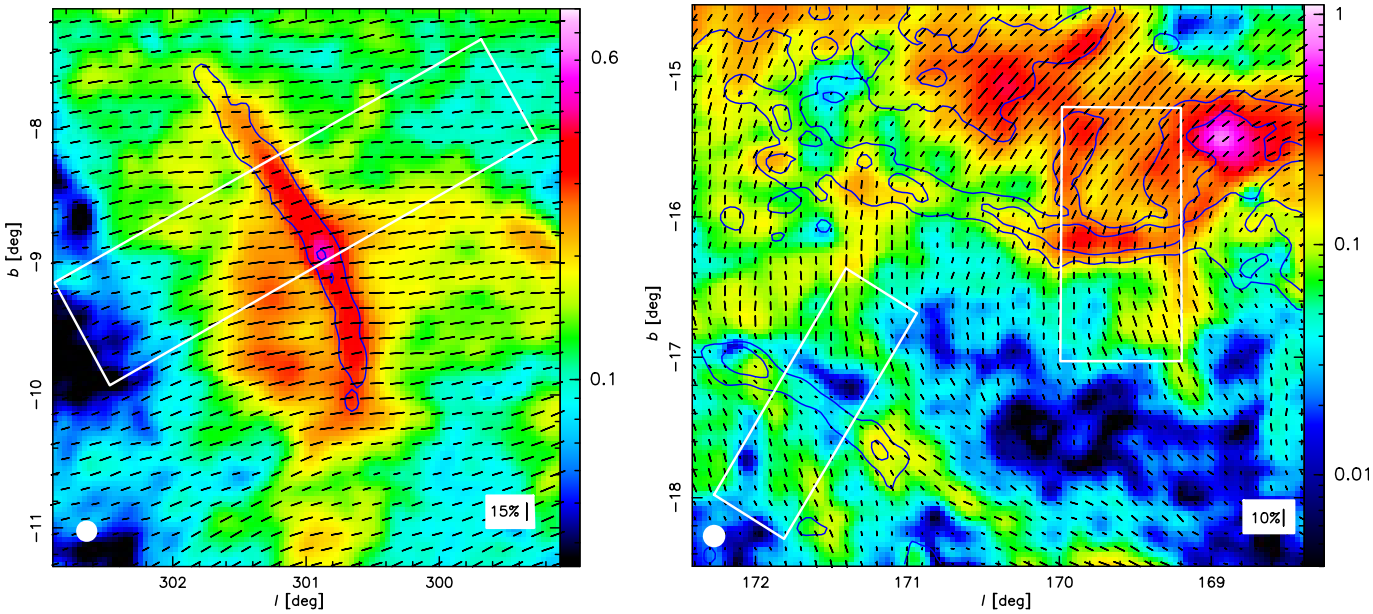

Fig. 7. Observed polarized emission at 353 GHz (in MJy sr^{-1}) of the Musca (*left*) and Taurus (*right*) clouds. The maps are at the resolution of 9.′6 (indicated by the white filled circles) for increased S/N. The black segments show the $\boldsymbol{B}_{\rm POS}$-field orientation (ψ+90°). The length of the pseudo-vectors is proportional to the polarization fraction. The blue contours show the total dust intensity at levels of 3 and 6 MJy sr^{-1}, at the resolution of 4.′8. The white boxes correspond to the area of the filaments and their backgrounds that is analysed in the rest of the paper.

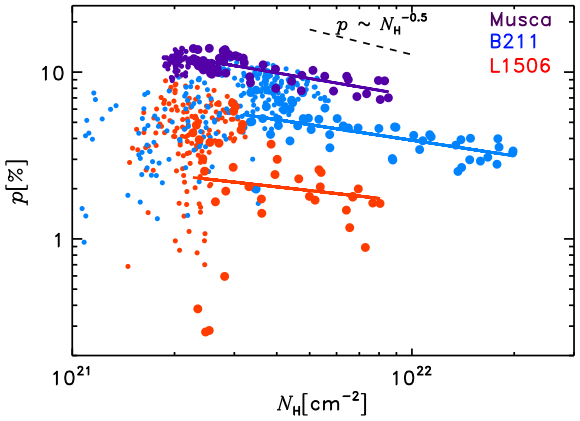

Fig. 8. Observed polarization fraction (p) as a function of column density ($N_{\rm H}$), for the cuts across the crest of the filaments derived from the boxes shown in Fig. 7. The small and large dots correspond to the background and filament regions, respectively. The three lines show linear fits for the filament regions of log p versus log $N_{\rm H}$ described in Sect. 3.4. The data uncertainties depend on the intensity of the polarized emission. They are the largest for low p and $N_{\rm H}$ values. The mean errorbar on p is 1.2% for the data points used for the linear fits. For smaller $N_{\rm H}$ values, the uncertainty on p is larger but does not account for the full dispersion of the data points.

allows us to characterize and compare the polarization properties of each emission component (Sects. 4.2 and 4.3).

4.1. A two-component model: filament and background

The observed polarized emission results from the integration along the LOS of the Stokes parameters. We take this into account by separating the filament and background emission using the spatial information of the *Planck* maps. We describe the dust emission observed towards the filaments as a simplified model with two components. One component corresponds to the filament, for $|r| < R_{\rm out}$, where r is the radial position relative to the filament crest ($r = 0$) and $R_{\rm out}$ is the outer radius. The other component represents the background.

We define as *background* the emission that is observed in the vicinity of a filament. It comprises the emission from the molecular cloud where the filament is located and from the diffuse ISM on larger scales. We argue that the former is the dominant contribution. Indeed, the Taurus B211 and L1506 filaments and the lower column density gas surrounding them are detected at similar velocities in ^{13}CO and ^{12}CO (between 2 and 9 km s^{-1}, Goldsmith et al. 2008), indicating that most of the background emission is associated with the filaments. CO emission is also detected around the Musca filament (Mizuno et al. 2001). Planck Collaboration Int. XXVIII (2015) present a map of the dark neutral medium in the Chameleon region derived from the comparison of γ-ray emission measured by *Fermi* with H I and CO data. This map shows emission around the Musca filament indicating that the background is not associated with the diffuse ISM traced by H I emission.

We separate the filament and background contributions to the I, Q, and U maps within the three fields defined by the white boxes in the Taurus and Musca images displayed in Fig. 7. The filaments have all a constant orientation on the POS within the selected fields. For L1506 the field also excludes the star-forming parts of that filament (see Sect. 3.3). Within each field, we separate pixels between filament and background areas using the I map to delineate the position and width of the filament. We fit the pixels over the background area with a polynomial function in the direction perpendicular to the filament crest. The fits account for the variations of the background emission, most noticeable for U in B211 (see Fig. 4). The spatial separation is illustrated on the I, Q, and U radial profiles shown in Fig. 9. These mean profiles are obtained by averaging data within the selected fields in the direction parallel to the filament crests. They are related to the profiles presented in Sect. 3 as follows. The mean profile of Musca corresponds to the averaging of profiles 4 and 5

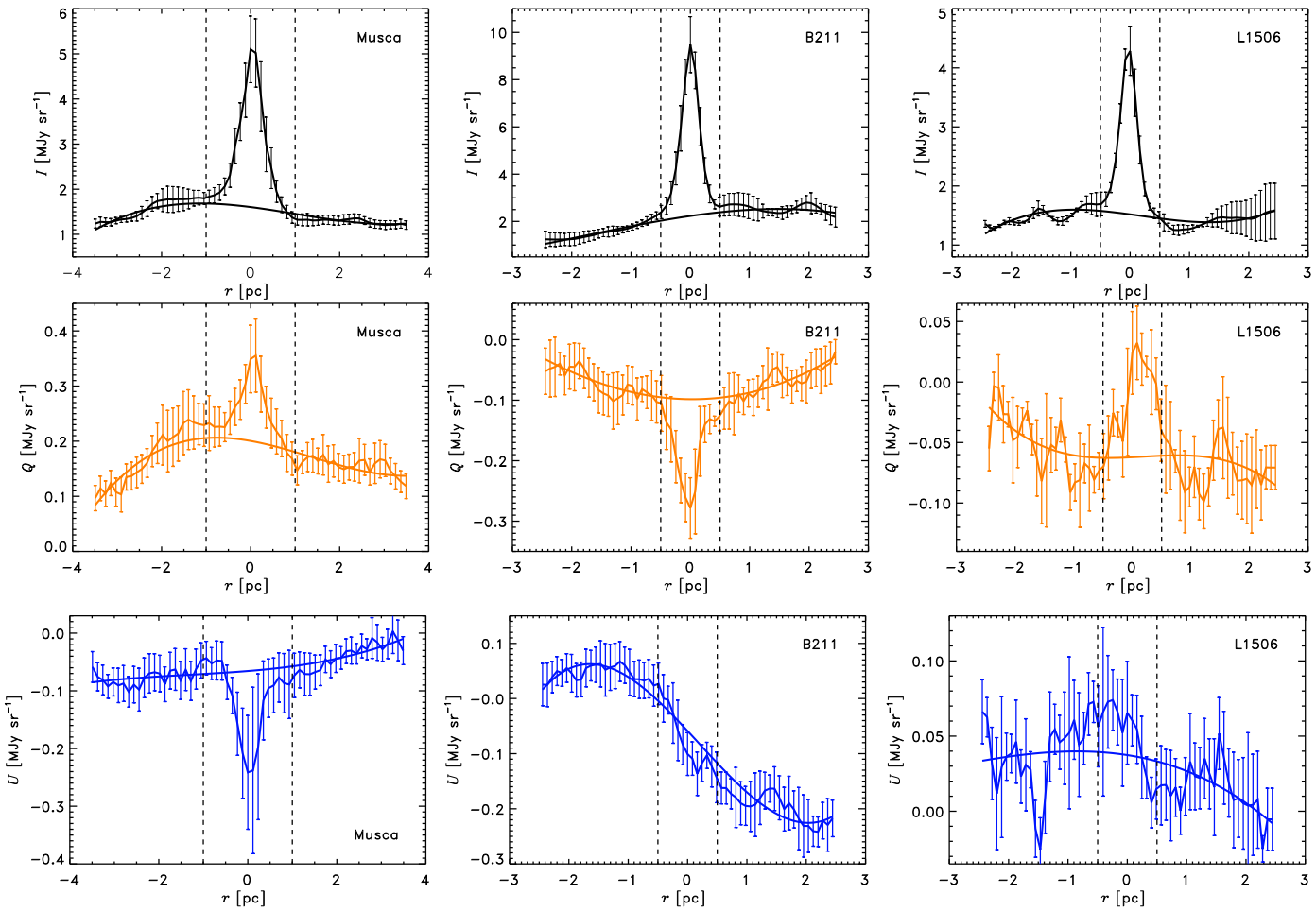

Fig. 9. Stokes parameters observed towards Musca (*left*), B211(*middle*), and L1506 (*right*). The profiles correspond to the observed I (*top*), Q (*middle*) and U (*bottom*) emission averaged along the filament crest as explained in Sect. 4.1. The errorbars represent the dispersion of the pixel values that have been averaged at a given r. The polynomial fits to the background are also shown. The vertical dashed lines indicate the position of the outer radius $R_{\rm out}$ for each filament.

in Fig. 2, that of the B211 filament to profiles 1 to 4 in Fig. 5, and for L1506 to the profiles 2 to 4 in Fig. 6. Figure 9 gives the fits of the I, Q, and U profiles for $|r| > R_{\rm out}$ with polynomial functions of degree three and interpolated for $|r| < R_{\rm out}$. The fits reproduce well the variations of the background emission outside of the filaments (Fig. 9).

4.2. Derivation of the polarization properties

We use the spatial separation of the filament and background contributions to the Stokes maps to derive the polarization properties of the filaments and their backgrounds listed in Table 2. We detail how the various entries in the Table have been computed.

The fits provide estimates of the background values interpolated at $r = 0$. The entries $I_{\rm bg}$, $Q_{\rm bg}$, and $U_{\rm bg}$ in Table 2 are mean values averaged along the filament crests. The polarization angles ($\psi_{\rm bg}$) and fractions ($p_{\rm bg}$) for the background are computed from $I_{\rm bg}$, $Q_{\rm bg}$, and $U_{\rm bg}$. The errorbars are statistical uncertainties. There is also an uncertainty associated with our specific choice for the degree of the polynomial function, which we quantify giving values derived from a third degree polynomial (pol3) and a linear (pol1) fit of the background. To compute the dispersion of the polarization angle ($\sigma_{\psi_{\rm bg}}$), we smooth the Q and U background subtracted maps with a 3×3 pixels boxcar average. The values of $\sigma_{\psi_{\rm bg}}$ in Table 2 are noise corrected. They correspond to the square root of the difference between the variance of the polarization angles on the background and that of the noise. The noise variance is computed from the dispersion of Q and U in reference, low brightness, areas within the Taurus and Musca maps, outside the molecular clouds. It comprises both the data noise and the fluctuations of the Galactic emission. The uncertainty on the noise correction is not a significant source of error on $\sigma_{\psi_{\rm bg}}$ after smoothing the data with a 3×3 pixels boxcar. We have also checked that we obtain values for $\sigma_{\psi_{\rm bg}}$ within the quoted errorbars using a 5×5 pixels boxcar average.

We compute the filament I, Q, and U emission averaging pixels of the background-subtracted maps along cuts perpendicular to the filament. The data averaging, done to reduce the noise, yields about 20 values of each Stokes parameters along the crest of each filament, spaced by $2'$ for an angular resolution of $4.'8$. The mean Stokes parameters ($I_{\rm fil}$, $Q_{\rm fil}$, and $U_{\rm fil}$), the mean values of the intrinsic polarization angle ($\psi_{\rm fil}$) and fraction ($p_{\rm fil}$), the dispersion $\sigma_{\psi_{\rm fil}}$, and their error bars are computed from the average and the dispersion of these values. In Table 2, we also list the polarization properties computed for the total filament emission without background subtraction (i.e., the observed emission towards the filament). The values of $\sigma_{\psi_{\rm fil}}$ are systematically greater with than without background subtraction because the dispersion

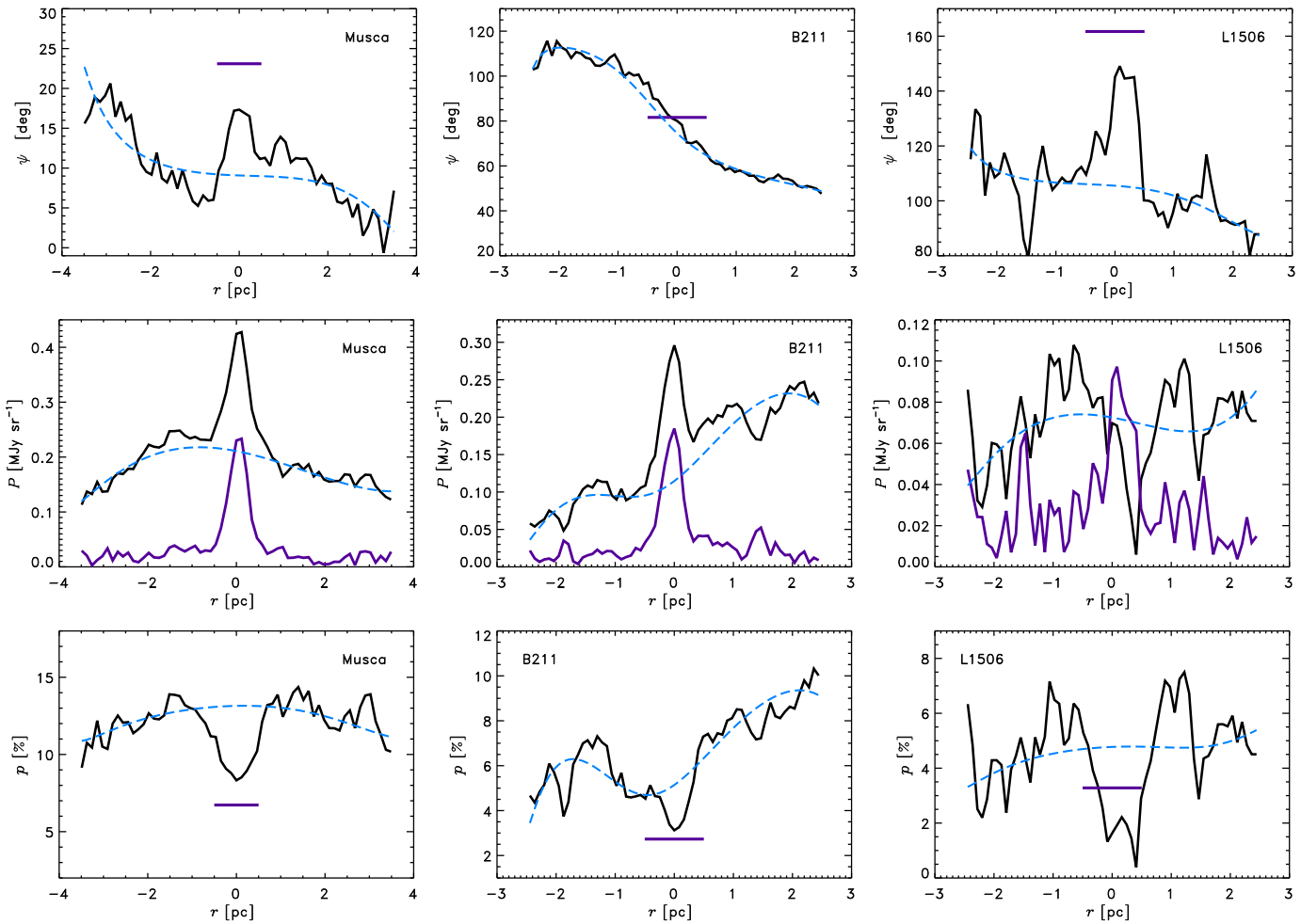

Fig. 10. Observed profiles (in black) of the polarization angle, the polarized intensity, and the polarization fraction, *from top to bottom*. The dashed blue curves show the variation of the background values of $\psi_{\rm bg}$, $P_{\rm bg}$, and $p_{\rm bg}$ derived from $I_{\rm bg}$, $Q_{\rm bg}$, and $U_{\rm bg}$. On the *middle three plots*, the $P_{\rm fil}$ profiles in purple are derived from the polynomial fits $I_{\rm fil}$, $Q_{\rm fil}$, and $U_{\rm fil}$. On the *top and bottom plots*, the horizontal purple lines indicate the mean values of the intrinsic polarization angle and fraction of the filaments for $|r| \leq R_{\rm out}$.

of polarization angles depend on the intensity of the polarized emission, which is reduced by the subtraction of the background.

The data analysis is illustrated in two figures. The profiles of the polarization angle, the total polarized intensity, and the polarization fraction derived from the data and the fits to the background are shown in Fig. 10. This figure also shows the intrinsic polarized intensity of the filament after subtraction of the background emission. Figure 11 shows the profile of $\psi_{\rm fil}$ along and across each of the three filaments.

4.3. Comparing the filament properties with that of their backgrounds

We use the results of our data analysis to compare the polarization properties of the filaments to those of their backgrounds.

Figures 10 and 11 show that for the three filaments, $\psi_{\rm fil}$ differs from $\psi_{\rm bg}$ by 12°, 6° and 54° for the Musca, B211 and l1506 filaments, respectively (see Table 2). In Appendix A, we compute analytically the polarized emission resulting from the superposition along the LOS of two emission components with different polarization angles. This analytical model is used to compute the observed polarization angle and fraction of the total emission as a function of the polarized intensity contrast and the difference in polarization angles. In the observations, the two components represent the filament and its background. Like in the model, the observed polarization angle derived from the total emission at the position of the filament (without background subtraction) differs from $\psi_{\rm fil}$. The difference of 29° for L1506 is in good agreement with the value for the analytical model in Fig. A.1 for $\Delta\psi = 54°$ and equal contributions of the filament and background to the polarized emission.

The LOS integration of both components, for $\psi_{\rm fil} \neq \psi_{\rm bg}$, always depolarizes the total emission. This effect has been ignored in earlier studies because it cannot be easily taken into account with stellar and sub-mm ground-based polarization observations. The L1506 filament illustrates the depolarization that results from the integration of the emission along the LOS: the polarized emission peaks at the position of the filament only after subtraction of the background (Fig. 10). For each of the filaments the effect of the LOS integration on p is different. The polarization fractions of the filaments are smaller than the values derived from the total emission for Musca and B211, while for L1506 it is greater. For the three filaments, the polarization fraction is smaller than that of the background interpolated at $r = 0$, as can be read in the right column of Table 2 and seen in the bottom row of Fig. 10, but this decrease is small for L1506 ($p_{\rm fil} = 3.3 \pm 0.3$ versus $p_{\rm bg} = 3.9 \pm 0.3$). In Appendix A.2, we compute the depolarization factor F as a function of the

Table 2. Polarization properties of the Musca, B211, and L1506 filaments (Fil) and their backgrounds (Bg).

	I [MJy sr^{-1}]	Q [MJy sr^{-1}]	U [MJy sr^{-1}]	ψ^a [deg]	$\sigma_\psi{}^b$ [deg]	p [%]
Musca						
Total	3.67 ± 0.04	0.29 ± 0.01	−0.17 ± 0.01	15.4 ± 0.5	2.1 ± 0.3	9.1 ± 0.5
Fil(pol3)	2.12 ± 0.04	0.11 ± 0.01	−0.11 ± 0.01	22.2 ± 1.3	5.1 ± 0.6	7.3 ± 0.4
Fil(pol1)	2.39 ± 0.05	0.15 ± 0.01	−0.12 ± 0.01	19.3 ± 1.0	3.8 ± 0.4	8.2 ± 0.4
Bg(pol3)	1.55 ± 0.01	0.18 ± 0.01	−0.06 ± 0.01	9.8 ± 0.3	2.7 ± 0.2	12.1 ± 0.1
Bg(pol1)	1.28 ± 0.01	0.13 ± 0.01	−0.05 ± 0.01	10.0 ± 0.4	3.8 ± 0.2	11.2 ± 0.1
B211						
Total	7.31 ± 0.19	−0.24 ± 0.01	−0.11 ± 0.01	77.9 ± 0.8	3.5 ± 0.4	3.5 ± 0.2
Fil(pol3)	4.50 ± 0.19	−0.12 ± 0.01	−0.04 ± 0.01	81.0 ± 1.8	7.8 ± 0.9	2.7 ± 0.2
Fil(pol1)	4.86 ± 0.19	−0.14 ± 0.01	−0.03 ± 0.01	84.7 ± 1.6	6.7 ± 0.8	2.9 ± 0.2
Bg(pol3)	2.81 ± 0.03	−0.12 ± 0.01	−0.07 ± 0.01	75.3 ± 0.8	5.7 ± 0.6	4.9 ± 0.2
Bg(pol1)	2.45 ± 0.02	−0.10 ± 0.01	−0.07 ± 0.01	70.1 ± 1.0	7.9 ± 0.6	5.1 ± 0.1
L1506						
Total	3.28 ± 0.09	−0.01 ± 0.01	0.07 ± 0.01	132.3 ± 2.5	6.5 ± 2.0	2.1 ± 0.2
Fil(pol3)	1.69 ± 0.08	0.04 ± 0.01	0.03 ± 0.01	161.7 ± 3.4	9.9 ± 2.4	3.3 ± 0.3
Fil(pol1)	1.77 ± 0.09	0.05 ± 0.01	0.03 ± 0.01	164.0 ± 2.8	7.8 ± 2.1	3.6 ± 0.4
Bg(pol3)	1.59 ± 0.03	−0.05 ± 0.01	0.04 ± 0.01	107.8 ± 2.3	15.1 ± 1.5	3.9 ± 0.3
Bg(pol1)	1.50 ± 0.02	−0.06 ± 0.01	0.04 ± 0.01	105.2 ± 2.0	13.5 ± 1.3	4.7 ± 0.2

Notes. The total and filament values are computed on maps without and with background subtraction, respectively. They are average values across the filament area as explained in Sect. 4.2. The background values are at $r = 0$. We give two sets of values derived from the polynomial fits of degree three (pol3) and one (pol1) for comparison. $^{(a)}$ The errors on the polarization angles, ψ, correspond to statistical errors on the mean value of ψ. $^{(b)}$ The dispersion of the polarization angles, σ_ψ, are derived as explained in Sect. 4.2.

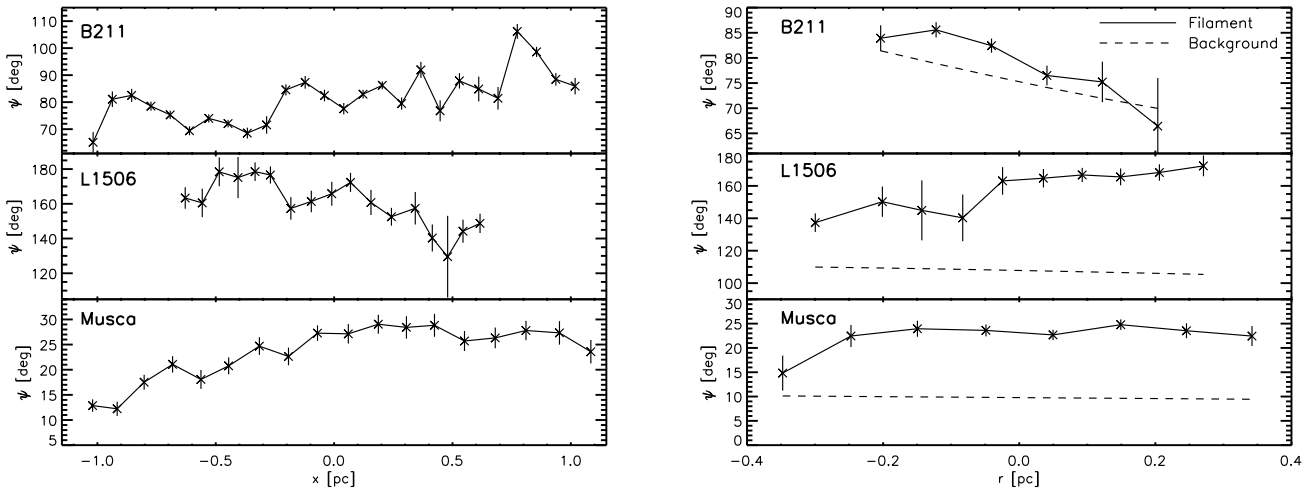

Fig. 11. Filament intrinsic polarization angle along (*left panel*), and perpendicular (*right panel*) to, the crests of the filaments. The crosses are data points computed from Q and U values, after averaging the background subtracted maps in the direction perpendicular (*left panel*) and parallel (*right*) to the filament crests. In the *left panel*, x is a coordinate along the filament crest, while in the *right panel*, r is the radial distance to the filament crests. In the *right panel*, the dashed line represents the background polarization angle. The beam is 0.3 pc for Musca, and 0.2 pc for B211 and L1506.

polarization angle difference and of the polarized intensity contrast. Figure A.2 shows that for $\Delta\psi = 54°$, $F \simeq 0.6$ for comparable contributions of the filament and background to the polarized emission as in L1506 (see P profile in Fig. 10). This factor is in good agreement with the ratio between the two p values, without and with background subtraction, for L1506 in Table 2.

The differences between the filament position angles (PA) and χ (ψ + 90°) are listed in Table 3. We find that $\boldsymbol{B}_{\rm POS}$ in the backgrounds of Musca and B211 are close, within 20°, to being orthogonal to the filament crest, while for L1506, the background $\boldsymbol{B}_{\rm POS}$ is at 37°. In the filaments, $\boldsymbol{B}_{\rm POS}$ is perpendicular within 10° to the crest of Musca and B211, while it is close to parallel in L1506. We point out, however, that two orientations that are nearly perpendicular in 3D may be close to parallel on the POS (Planck Collaboration Int. XXXII 2016; Planck Collaboration Int. XXXV 2016).

5. Interpretation of the polarization fraction

We discuss possible interpretations of the polarization fraction and its variation from the backgrounds to the filaments. The polarization fraction depends on dust grain properties and

on the magnetic field structure expressed as the sum of mean and turbulent components. The observed polarization fraction is empirically parametrized as

$$p = p_{\rm dust}\, R\, F\, \cos^2\gamma, \tag{6}$$

to distinguish four different effects due to both the local properties of dust and magnetic fields, and the LOS integration. The polarization properties of dust are taken into account with $p_{\rm dust}$ that depends on the composition, size, and shape of dust grains (Lee & Draine 1985; Hildebrand 1988). The Rayleigh reduction factor, $R \leq 1$, characterizes the efficiency of grain alignment with the local magnetic field orientation. The factor F expresses the impact on the polarization fraction of the variation of the magnetic field orientation along the LOS and within the beam. The role of the orientation of the mean magnetic field with respect to the POS is expressed by the $\cos^2\gamma$ factor. The polarization fraction is maximal when the magnetic field is uniform and in the POS ($\gamma = 0$), while there is no linear polarization if the magnetic field is along the LOS ($\gamma = 90°$). A main difficulty in the interpretaion of polarization observations is that these four quantities cannot be determined independently. In particular, the product $p_{\rm dust}\, R\, F$ is degenerated with the orientation of the mean magnetic field.

The interpretation of the polarization fraction presented in Sect. 5.1 focuses on the structure of the magnetic field. The factors $p_{\rm dust}$ and R are discussed in Sect. 5.2.

5.1. The structure of the magnetic field

5.1.1. Mean magnetic field orientation

For each of the three filaments, we find that the polarization angles vary from the background to the filament. These variations reflect changes in the 3D structure of the magnetic field, which affect p in two ways. First, changes of ψ along the LOS depolarize the emission lowering the observed p (see Appendix A). Second, p depends on the angle of $\boldsymbol{B}$ with respect to the POS (γ), which statistically must vary as much as ψ. We quantify these two aspects.

(1) L1506 illustrates the depolarization due to the superposition of emitting layers with different polarization angles (Sect. 4.3). For this filament, the decrease in p versus $N_{\rm H}$ in Fig. 8 can be almost entirely explained by the change of the $\boldsymbol{B}_{\rm POS}$ orientation between the filament and its background. For Musca and B211, the ψ differences are too small to account for the observed decrease in p in the filaments (see Fig. A.2).

(2) The smooth variations of $\psi_{\rm bg}$ in the background of B211 and Musca, by about 60° and 20° respectively, are associated with variations of p by 3–5 % (Fig. 10). The variations of ψ are likely to be associated with variations of γ of comparable amplitude that could contribute to the variations of p. The difference of p at a given $N_{\rm H}$ for the three filaments in Fig. 8 may indicate changes of the mean orientation of $\boldsymbol{B}$ with respect to the POS. We build on this idea to quantify the variations of γ that would be needed to account for the difference between p values for the filament and the background (at $r = 0$), $p_{\rm fil}$ and $p_{\rm bg}$, listed in Table 2. The angles $\gamma_{\rm fil}$ and $\gamma_{\rm bg}$ of $\boldsymbol{B}$ with respect to the POS for the filament and the background are calculated, within the range 0° to 90°, from Eq. (6) written as

$$p = p_0 \cos\gamma^2, \tag{7}$$

Table 3. Estimated angle differences.

	$p_0^{{\rm bg}\,a}$	$\Delta\gamma$ [deg]	$\Delta\chi$ [deg]	$\lvert\chi_{\rm fil} - {\rm PA}\rvert$ [deg]	$\lvert\chi_{\rm bg} - {\rm PA}\rvert$ [deg]
Musca . .	0.12–0.2	39–14	12	82	70
B211 . . .	0.049–0.2	42–8	6	81	75
L1506 . .	0.039–0.2	25–3	54	17	37

Notes. Columns 2 and 3 give the values of $p_0^{\rm bg}$ and the corresponding $\Delta\gamma = \gamma_{\rm fil} - \gamma_{\rm bg}$ computed for $p_0^{\rm bg} = p_0^{\rm fil}$ (see Sect. 5.1.1). Column 4 gives the values of $\Delta\chi = |\chi_{\rm fil} - \chi_{\rm bg}|$ corresponding to the $\psi_{\rm fil}$ and $\psi_{\rm bg}$ values of Table 2 for the polynomial fits (pol3). Columns 5 and 6 give the relative angle between the PA of the filament and the $\boldsymbol{B}_{\rm POS}$ angle in the filament and in the background, respectively. The PA of the filaments are given in Table 1. [(a)] The smallest value of $p_0^{\rm bg}$ is the observed $p_{\rm bg}$. The maximum value of 0.2 is close to the maximum dust polarization fraction observed by *Planck* at 353 GHz (Planck Collaboration Int. XIX 2015).

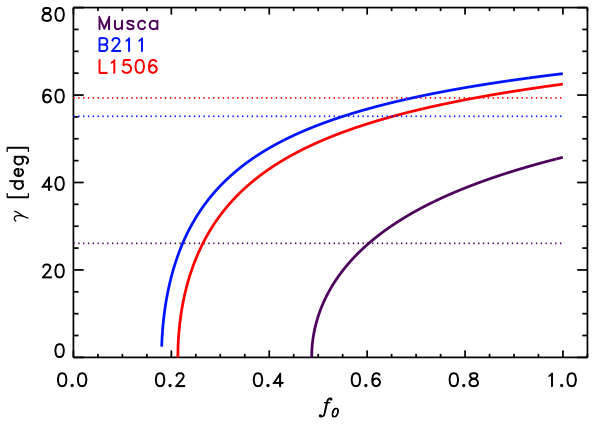

Fig. 12. Angles of $\boldsymbol{B}$ with respect to the POS $\gamma_{\rm bg}$ (dotted line) and $\gamma_{\rm fil}$ (solid line) computed with Eq. (7), as a function of $f_0 = p_0^{\rm fil}/p_0^{\rm bg}$ for $p_0^{\rm bg} = 0.15$.

where $p_0 = p_{\rm dust}\, R\, F$ may differ between the filament ($p_0^{\rm fil}$) and the background ($p_0^{\rm bg}$). The difference $\Delta\gamma = \gamma_{\rm fil} - \gamma_{\rm bg}$ depends on both $p_0^{\rm bg}$ and $f_0 = p_0^{\rm fil}/p_0^{\rm bg}$. For illustration we discuss two cases. First, in Table 3 for $f_0 = 1$, we give two values of $\Delta\gamma$ computed for extreme values of $p_0^{\rm bg}$: the minimum value set by the observed polarization fraction at $r = 0$ and a maximum value of 0.2. Second, in Fig. 12, we plot $\gamma_{\rm bg}$ and $\gamma_{\rm fil}$ versus f_0 for $p_0^{\rm bg} = 0.15$. In this figure, the sign of $\Delta\gamma$ changes from negative to positive at different values of f_0 for each of the filaments. The orientation of $\boldsymbol{B}$ contributes to the decrease in the polarization fraction in the filament when $\Delta\gamma > 0$, i.e., $\boldsymbol{B}$ is closer to the LOS in the filament than in the background. By no way, this could be the rule to explain the low values of the polarization fraction that have been observed in other filaments (e.g., Goodman et al. 1995; Sugitani et al. 2011; Cashman & Clemens 2014). We conclude that other factors than the mean magnetic field orientation contribute to the decrease in p in the filaments.

5.1.2. Fluctuation of the magnetic field orientation

Depolarization in filaments could result from the integration along the LOS of a large number of emission layers with

different orientations of the magnetic field. Assuming the number of layers is proportional to the total column density $N_{\rm H}$ (Myers & Goodman 1991), we expect p to decrease with increasing $N_{\rm H}$ due to the averaging of the random component of the magnetic field (Jones et al. 2015). These models depend on the ratio between the strength of the random and of the mean components of the magnetic field (Jones et al. 1992). The steepest dependence, p scaling as $N_{\rm H}^{-0.5}$, is obtained when the random component is dominant, in which case the dispersion of the polarization angle reaches its maximum value $\sigma_\psi^{\rm max}$ of 52° (Planck Collaboration Int. XIX 2015). In such a model, we expect the dispersion of ψ to be close to $\sigma_\psi^{\rm max}$ in the background and much smaller in the filament (see Fig. 9 in Jones et al. 1992). This prediction is inconsistent with our data because (1) $\sigma_{\psi_{\rm bg}}$ is much smaller than $\sigma_\psi^{\rm max}$ and (2) it is comparable to and even smaller than $\sigma_{\psi_{\rm fil}}$ (Table 2).

Moreover Fig. 11 shows that the variations of the magnetic field orientation are not random. Systematic variations of the polarization angle along and across the filaments must also exist on scales unresolved by *Planck* observations. Hence, we expect some depolarization from coherent changes of the field orientation in the beam and along the LOS. Spectroscopic observations of B211 show density and velocity structures on scales five times smaller than the *Planck* beam, and coherent over lengths of ~0.4 pc, i.e., two *Planck* beams (Hacar et al. 2013). Similar structures are anticipated to exist for the magnetic field.

Theoretical modelling is warranted to quantify the depolarization within the beam and along the LOS, and to test whether the structure of the magnetic field may account for the observed decrease in p in the filaments (see Sect. 3.4 and Fig. 8). The decrease in p due to the structure of the magnetic field has already been quantified for helical fields (e.g., Carlqvist & Kristen 1997; Fiege & Pudritz 2000). Other models could be investigated such as the magneto-hydrostatic configuration presented by Tomisaka (2014). Tomisaka (2015) describes the change in the polarization angle and the decrease in the polarization fraction produced by the pinching of the $\boldsymbol{B}$-field lines by gravity within this model. Since the angular resolution of *Planck* does not resolve the inner structure of the filaments, observations with a higher angular resolution would be needed to fully test such models. This is the research path to understanding the role played by the magnetic field in the formation of star-forming filaments.

5.2. Grain alignment efficiency and dust growth

Different mechanisms have been proposed to explain how the spin axes of grains can become aligned with the magnetic field. Alignment could result from magnetic relaxation (Davis & Greenstein 1951; Jones & Spitzer 1967; Purcell 1979; Spitzer & McGlynn 1979). However, the most recent theory stresses the role of radiative torques (RAT, Dolginov & Mitrofanov 1976; Draine & Weingartner 1996, 1997; Lazarian et al. 1997; Lazarian 2007; Lazarian & Hoang 2007; Hoang & Lazarian 2014). A number of studies interpret polarization observations in the framework of this theory (Gerakines et al. 1995; Whittet et al. 2001, 2008; Andersson & Potter 2010; Andersson et al. 2011, 2013; Cashman & Clemens 2014). The observed drop of p with column density has been interpreted as evidence of the progressive loss of grain alignment with increasing column density (Andersson 2015). However, this interpretation cannot be validated without also considering the impact of gas density on the grain size and shape.

Dust observations, both in extinction and in emission, provide a wealth of evidence of grain growth in dense gas within molecular clouds (e.g., Ysard et al. 2013; Roy et al. 2013; Lefèvre et al. 2014, as recent references). This increase in the typical size of large grains may contribute to the observed dependence of $\lambda_{\rm max}$, the peak of the polarization curve in extinction, on the visual extinction $A_{\rm V}$ (Wurm & Schnaiter 2002; Voshchinnikov et al. 2013; Voshchinnikov & Hirashita 2014). Dust growth through coagulation and accretion also modifies the shape of grains, therefore their polarization cross-sections, and $p_{\rm dust}$. So the study of the variation of polarization with $A_{\rm V}$ in dense shielded regions requires the modelling of both grain growth and alignment efficiency. Grain growth may allow for a sustained alignment up to high column densities (Andersson 2015). Thus, the product $p_{\rm dust}R$ may not be changing much from the backgrounds to the filaments.

6. Conclusions

We have presented and analysed the *Planck* dust polarization maps towards three nearby star-forming filaments: the Musca, B211, and L1506 filaments.These filaments can be recognized in the maps of intensity and Stokes Q and U parameters. We use these maps to separate the filament emission from its background, and infer the structure of the magnetic field from the polarization properties. This focused study complements statistical analysis of *Planck* polarization observations of molecular clouds (Planck Collaboration Int. XX 2015; Planck Collaboration Int. XXXII 2016; Planck Collaboration Int. XXXV 2016).

Planck images allow us to describe the observed Stokes parameters with a two-component model, the filaments and their backgrounds. We show that it is important to remove the background emission in all three Stokes parameters, I, Q, and U to properly measure the polarization properties (p and ψ) intrinsic to the filaments. Both the polarization angle and fraction measured at the intensity peak of the filaments differ from their intrinsic values.

In all three cases, we measure variations in the polarization angle of the filaments ($\psi_{\rm fil}$) with respect to that of their backgrounds ($\psi_{\rm bg}$) and these variations are found to be coherent along the pc-scale length of the filaments. The differences between $\psi_{\rm fil}$ and $\psi_{\rm bg}$ for two of the three filaments are larger than the dispersion of the polarization angles. Hence, these differences are not random fluctuations and they indicate a change in the orientation of the POS component of the magnetic field between the filaments and their backgrounds. We also observe coherent variations of ψ across the background and within the filaments. These observational results are all evidence of changes of the 3D magnetic field structure.

Like in earlier studies, we find a systematic decrease in the polarization fraction for increasing gas column density. For L1506 the change of ψ in the filament with respect to that of the background accounts for most of the observed drop of p in the filament. From this example, we argue that the magnetic field structure contributes to the observed decrease in the polarization fraction in the filaments. We show that the depolarization in the filaments cannot be due to random fluctuations of ψ because (1) the dispersion of ψ is small (10°) and much smaller than the value of 52° for a random distribution; and (2) it is comparable in the filaments and their corresponding backgrounds. The ordered magnetic fields implied by the small dispersion of the polarization angle measured inside and around the three filaments are in agreement with the ordered morphology of magnetic fields observed from 100 pc to sub-pc scales (see, e.g., Li et al. 2014).

Variations of the angle of $\boldsymbol{B}$ with respect to the POS cannot explain the systematic decrease in p with $N_{\rm H}$ either, but unresolved structure of the magnetic field within the filaments may contribute to that decrease. Indeed, we find that the dispersion of ψ in the filaments is comparable to, and even larger than, that in the background. These fluctuations of ψ are not random but due to coherent variations along and across the filaments that trace the structure of the magnetic field within the filaments. The drop in p expected from the magnetic field structure does not preclude some contribution from variations of grain alignment with column density. Theoretical modelling is needed to test whether the inner structure of the magnetic field may account for the observed decrease in p in the filaments. Modelling is also crucial to quantify the role that the magnetic field plays in the formation and evolution of star-forming filaments.

Further analyses of a larger sample of filaments observed by *Planck*, but also higher angular resolution observations, are required to investigate the magnetic field structure in filaments. More extensive molecular line mapping of a larger sample of filaments is very desirable, in order to set stronger observational constraints on the dynamics of these structures, as well as to investigate the link between the velocity and the magnetic fields in molecular clouds. Comparison with dedicated numerical simulations will also be valuable in our understanding and interpretation of the observational results.

Acknowledgements. The Planck Collaboration acknowledges the support of: ESA; CNES, and CNRS/INSU-IN2P3-INP (France); ASI, CNR, and INAF (Italy); NASA and DoE (USA); STFC and UKSA (UK); CSIC, MINECO, JA and RES (Spain); Tekes, AoF, and CSC (Finland); DLR and MPG (Germany); CSA (Canada); DTU Space (Denmark); SER/SSO (Switzerland); RCN (Norway); SFI (Ireland); FCT/MCTES (Portugal); ERC and PRACE (EU). A description of the Planck Collaboration and a list of its members, indicating which technical or scientific activities they have been involved in, can be found at http://www.cosmos.esa.int/web/planck/planck-collaboration. The research leading to these results has received funding from the European Research Council under the European Union's Seventh Framework Programme (FP7/2007-2013)/ERC grant agreement No. 267934.

References

Abergel, A., Boulanger, F., Mizuno, A., & Fukui, Y. 1994, ApJ, 423, L59
Andersson, B.-G. 2015, in Astrophys. Space Sci. Libr. 407, eds. A. Lazarian, E. M. de Gouveia Dal Pino, & C. Melioli, 59
Andersson, B.-G., & Potter, S. B. 2010, ApJ, 720, 1045
Andersson, B.-G., Pintado, O., Potter, S. B., Straižys, V., & Charcos-Llorens, M. 2011, A&A, 534, A19
Andersson, B.-G., Piirola, V., De Buizer, J., et al. 2013, ApJ, 775, 84
André, P., Men'shchikov, A., Bontemps, S., et al. 2010, A&A, 518, L102
André, P., Di Francesco, J., Ward-Thompson, D., et al. 2014, Protostars and Planets VI, 27
Arzoumanian, D., André, P., Didelon, P., et al. 2011, A&A, 529, L6
Attard, M., Houde, M., Novak, G., et al. 2009, ApJ, 702, 1584
Bally, J., Lanber, W. D., Stark, A. A., & Wilson, R. W. 1987, ApJ, 312, L45
Cambrésy, L. 1999, A&A, 345, 965
Carlqvist, P., & Kristen, H. 1997, A&A, 324, 1115
Cashman, L. R., & Clemens, D. P. 2014, ApJ, 793, 126
Chapman, N. L., Goldsmith, P. F., Pineda, J. L., et al. 2011, ApJ, 741, 21
Cox, N., Arzoumanian, D., Rygl, K., et al. 2015, A&A, submitted
Crutcher, R. M., Nutter, D. J., Ward-Thompson, D., & Kirk, J. M. 2004, ApJ, 600, 279
Davis, Jr., L., & Greenstein, J. L. 1951, ApJ, 114, 206
Dolginov, A. Z., & Mitrofanov, I. G. 1976, Ap&SS, 43, 291
Draine, B. T., & Weingartner, J. C. 1996, ApJ, 470, 551
Draine, B. T., & Weingartner, J. C. 1997, ApJ, 480, 633
Elias, J. H. 1978, ApJ, 224, 857
Falceta-Gonçalves, D., Lazarian, A., & Kowal, G. 2008, ApJ, 679, 537
Falceta-Gonçalves, D., Lazarian, A., & Kowal, G. 2009, in Rev. Mex. Astron. Astrofis. Conf. Ser., 36, 37
Falgarone, E., Pety, J., & Phillips, T. G. 2001, ApJ, 555, 178
Fiege, J. D., & Pudritz, R. E. 2000, ApJ, 544, 830
Franco, G. A. P. 1991, A&A, 251, 581
Gerakines, P. A., Whittet, D. C. B., & Lazarian, A. 1995, ApJ, 455, L171
Goldsmith, P. F., Heyer, M., Narayanan, G., et al. 2008, ApJ, 680, 428
Goodman, A. A., Bastien, P., Menard, F., & Myers, P. C. 1990, ApJ, 359, 363
Goodman, A. A., Jones, T. J., Lada, E. A., & Myers, P. C. 1995, ApJ, 448, 748
Górski, K. M., Hivon, E., Banday, A. J., et al. 2005, ApJ, 622, 759
Gregorio Hetem, J. C., Sanzovo, G. C., & Lepine, J. R. D. 1988, A&AS, 76, 347
Hacar, A., Tafalla, M., Kauffmann, J., & Kovács, A. 2013, A&A, 554, A55
Heyer, M., Gong, H., Ostriker, E., & Brunt, C. 2008, ApJ, 680, 420
Hildebrand, R. H. 1983, Quant. J. Roy. Astron. Soc., 24, 267
Hildebrand, R. H. 1988, QJRAS, 29, 327
Hily-Blant, P., & Falgarone, E. 2009, A&A, 500, L29
Hoang, T., & Lazarian, A. 2014, MNRAS, 438, 680
Joncas, G., Boulanger, F., & Dewdney, P. E. 1992, ApJ, 397, 165
Jones, R. V., & Spitzer, Jr., L. 1967, ApJ, 147, 943
Jones, T. J., Klebe, D., & Dickey, J. M. 1992, ApJ, 389, 602
Jones, T. J., Bagley, M., Krejny, M., Andersson, B.-G., & Bastien, P. 2015, AJ, 149, 31
Kenyon, S. J., Dobrzycka, D., & Hartmann, L. 1994, AJ, 108, 1872
Konyves, V., Andre, P., Men'shchikov, A., et al. 2015, A&A, 584, A91
Lazarian, A. 2007, J. Quant. Spectr. Rad. Transf., 106, 225
Lazarian, A., & Hoang, T. 2007, MNRAS, 378, 910
Lazarian, A., Goodman, A. A., & Myers, P. C. 1997, ApJ, 490, 273
Lee, H. M., & Draine, B. T. 1985, ApJ, 290, 211
Lefèvre, C., Pagani, L., Juvela, M., et al. 2014, A&A, 572, A20
Li, D., & Goldsmith, P. F. 2012, ApJ, 756, 12
Li, H.-B., Goodman, A., Sridharan, T. K., et al. 2014, Protostars and Planets VI, 101
Matthews, B. C., Wilson, C. D., & Fiege, J. D. 2001, ApJ, 562, 400
Matthews, B. C., McPhee, C. A., Fissel, L. M., & Curran, R. L. 2009, ApJS, 182, 143
Matthews, T. G., Ade, P. A. R., Angilè, F. E., et al. 2014, ApJ, 784, 116
McClure-Griffiths, N. M., Dickey, J. M., Gaensler, B. M., Green, A. J., & Haverkorn, M. 2006, ApJ, 652, 1339
Mizuno, A., Yamaguchi, R., Tachihara, K., et al. 2001, PASJ, 53, 1071
Molinari, S., Swinyard, B., Bally, J., et al. 2010, A&A, 518, L100
Montier, L., Plaszczynski, S., Levrier, F., et al. 2015, A&A, 574, A136
Motte, F., Zavagno, A., Bontemps, S., et al. 2010, A&A, 518, L77
Myers, P. C. 2009, A&A, 518, 1609
Myers, P. C., & Goodman, A. A. 1988, ApJ, 326, L27
Myers, P. C., & Goodman, A. A. 1991, ApJ, 373, 509
Nakamura, F., & Li, Z. 2008, ApJ, 687, 354
Ostriker, E. C., Stone, J. M., & Gammie, C. F. 2001, ApJ, 546, 980
Pagani, L., Ristorcelli, I., Boudet, N., et al. 2010, A&A, 512, A3
Palmeirim, P., André, P., Kirk, J., et al. 2013, A&A, 550, A38
Pascale, E., Ade, P. A. R., Angilè, F. E., et al. 2012, in SPIE Conf. Ser., 8444
Pereyra, A., & Magalhães, A. M. 2004, ApJ, 603, 584
Planck Collaboration I. 2014, A&A, 571, A1
Planck Collaboration II. 2014, A&A, 571, A2
Planck Collaboration XI. 2014, A&A, 571, A11
Planck Collaboration I. 2015, A&A, submitted [arXiv:1502.01582]
Planck Collaboration X. 2015, A&A, submitted [arXiv:1502.01588]
Planck Collaboration Int. XIX. 2015, A&A, 576, A104
Planck Collaboration Int. XX. 2015, A&A, 576, A105
Planck Collaboration Int. XXI. 2015, A&A, 576, A106
Planck Collaboration Int. XXII. 2015, A&A, 576, A107
Planck Collaboration Int. XXVIII. 2015, A&A, 582, A31
Planck Collaboration Int. XXIX. 2016, A&A, 586, A132
Planck Collaboration Int. XXX. 2016, A&A, 586, A133
Planck Collaboration Int. XXXII. 2016, A&A, 586, A135
Planck Collaboration Int. XXXV. 2016, A&A, 586, A138
Planck HFI Core Team 2011, A&A, 536, A4
Plaszczynski, S., Montier, L., Levrier, F., & Tristram, M. 2014, MNRAS, 439, 4048
Purcell, E. M. 1979, ApJ, 231, 404
Roy, A., Martin, P. G., Polychroni, D., et al. 2013, ApJ, 763, 55
Schlafly, E. F., Green, G., Finkbeiner, D. P., et al. 2014, ApJ, 786, 29
Schmalzl, M., Kainulainen, J., Quanz, S. P., et al. 2010, ApJ, 725, 1327
Schneider, S., & Elmegreen, B. G. 1979, ApJS, 41, 87
Shu, F. H., Adams, F. C., & Lizano, S. 1987, A&A, 25, 23
Sousbie, T. 2011, MNRAS, 414, 350
Spitzer, Jr., L., & McGlynn, T. A. 1979, ApJ, 231, 417
Stepnik, B., Abergel, A., Bernard, J.-P., et al. 2003, A&A, 398, 551
Sugitani, K., Nakamura, F., Watanabe, M., et al. 2011, ApJ, 734, 63

Tomisaka, K. 2014, ApJ, 785, 24
Tomisaka, K. 2015, ApJ, 807, 47
Voshchinnikov, N. V., & Hirashita, H. 2014, MNRAS, 445, 301
Voshchinnikov, N. V., Das, H. K., Yakovlev, I. S., & Il'in, V. B. 2013, Astron. Lett., 39, 421
Ward-Thompson, D., Kirk, J. M., Crutcher, R. M., et al. 2000, ApJ, 537, L135
Whittet, D. C. B., Gerakines, P. A., Hough, J. H., & Shenoy, S. S. 2001, ApJ, 547, 872
Whittet, D. C. B., Hough, J. H., Lazarian, A., & Hoang, T. 2008, ApJ, 674, 304
Wurm, G., & Schnaiter, M. 2002, ApJ, 567, 370
Ysard, N., Abergel, A., Ristorcelli, I., et al. 2013, A&A, 559, A133

[1] APC, AstroParticule et Cosmologie, Université Paris Diderot, CNRS/IN2P3, CEA/lrfu, Observatoire de Paris, Sorbonne Paris Cité, 10 rue Alice Domon et Léonie Duquet, 75205 Paris Cedex 13, France
[2] African Institute for Mathematical Sciences, 6–8 Melrose Road, Muizenberg, 7945 Cape Town, South Africa
[3] Agenzia Spaziale Italiana Science Data Center, via del Politecnico snc, 00133 Roma, Italy
[4] Aix Marseille Université, CNRS, LAM (Laboratoire d'Astrophysique de Marseille) UMR 7326, 13388 Marseille, France
[5] Astrophysics Group, Cavendish Laboratory, University of Cambridge, J J Thomson Avenue, Cambridge CB3 0HE, UK
[6] Astrophysics & Cosmology Research Unit, School of Mathematics, Statistics & Computer Science, University of KwaZulu-Natal, Westville Campus, Private Bag X54001, Durban 4000, South Africa
[7] CITA, University of Toronto, 60 St. George St., Toronto, ON M5S 3H8, Canada
[8] CNRS, IRAP, 9 Av. colonel Roche, BP 44346, 31028 Toulouse Cedex 4, France
[9] California Institute of Technology, Pasadena, California, USA
[10] Centro de Estudios de Física del Cosmos de Aragón (CEFCA), Plaza San Juan, 1, planta 2, 44001 Teruel, Spain
[11] Computational Cosmology Center, Lawrence Berkeley National Laboratory, Berkeley, CA 94720 California, USA
[12] Consejo Superior de Investigaciones Científicas (CSIC), Madrid, Spain
[13] DSM/Irfu/SPP, CEA-Saclay, 91191 Gif-sur-Yvette Cedex, France
[14] DTU Space, National Space Institute, Technical University of Denmark, Elektrovej 327, 2800 Kgs. Lyngby, Denmark
[15] Département de Physique Théorique, Université de Genève, 24 Quai E. Ansermet, 1211 Genève 4, Switzerland
[16] Departamento de Astrofísica, Universidad de La Laguna (ULL), 38206 La Laguna, Tenerife, Spain
[17] Departamento de Física, Universidad de Oviedo, Avda. Calvo Sotelo s/n, 33003 Oviedo, Spain
[18] Department of Astrophysics/IMAPP, Radboud University Nijmegen, PO Box 9010, 6500 GL Nijmegen, The Netherlands
[19] Department of Physics & Astronomy, University of British Columbia, 6224 Agricultural Road, Vancouver, British Columbia, Canada
[20] Department of Physics and Astronomy, Dana and David Dornsife College of Letter, Arts and Sciences, University of Southern California, Los Angeles, CA 90089, USA
[21] Department of Physics and Astronomy, University College London, London WC1E 6BT, UK
[22] Department of Physics, Florida State University, Keen Physics Building, 77 Chieftan Way, Tallahassee, Florida, USA
[23] Department of Physics, Gustaf Hällströmin katu 2a, University of Helsinki, 00100 Helsinki, Finland
[24] Department of Physics, Princeton University, Princeton, NJ 08544 New Jersey, USA
[25] Department of Physics, University of California, Santa Barbara, California, USA
[26] Department of Physics, University of Illinois at Urbana-Champaign, 1110 West Green Street, Urbana, Illinois, USA
[27] Dipartimento di Fisica e Astronomia G. Galilei, Università degli Studi di Padova, via Marzolo 8, 35131 Padova, Italy
[28] Dipartimento di Fisica e Scienze della Terra, Università di Ferrara, via Saragat 1, 44122 Ferrara, Italy
[29] Dipartimento di Fisica, Università La Sapienza, P.le A. Moro 2 Roma, Italy
[30] Dipartimento di Fisica, Università degli Studi di Milano, via Celoria, 16 Milano, Italy
[31] Dipartimento di Fisica, Università degli Studi di Trieste, via A. Valerio 2, 34128 Trieste, Italy
[32] Dipartimento di Fisica, Università di Roma Tor Vergata, via della Ricerca Scientifica, 1 Roma, Italy
[33] Dipartimento di Matematica, Università di Roma Tor Vergata, via della Ricerca Scientifica, 1 Roma, Italy
[34] Discovery Center, Niels Bohr Institute, Blegdamsvej 17, Copenhagen, Denmark
[35] European Space Agency, ESAC, Planck Science Office, Camino bajo del Castillo, s/n, Urbanización Villafranca del Castillo, Villanueva de la Cañada, 28692 Madrid, Spain
[36] European Space Agency, ESTEC, Keplerlaan 1, 2201 AZ Noordwijk, The Netherlands
[37] Facoltà di Ingegneria, Università degli Studi e-Campus, via Isimbardi 10, 22060 Novedrate (CO), Italy
[38] Gran Sasso Science Institute, INFN, viale F. Crispi 7, 67100 L'Aquila, Italy
[39] HGSFP and University of Heidelberg, Theoretical Physics Department, Philosophenweg 16, 69120 Heidelberg, Germany
[40] Helsinki Institute of Physics, Gustaf Hällströmin katu 2, University of Helsinki, Helsinki, Finland
[41] INAF–Osservatorio Astronomico di Padova, Vicolo dell'Osservatorio 5, Padova, Italy
[42] INAF–Osservatorio Astronomico di Roma, via di Frascati 33, Monte Porzio Catone, Italy
[43] INAF–Osservatorio Astronomico di Trieste, via G.B. Tiepolo 11, Trieste, Italy
[44] INAF/IASF Bologna, via Gobetti 101, Bologna, Italy
[45] INAF/IASF Milano, via E. Bassini 15, Milano, Italy
[46] INFN, Sezione di Bologna, via Irnerio 46, 40126 Bologna, Italy
[47] INFN, Sezione di Roma 1, Università di Roma Sapienza, Piazzale Aldo Moro 2, 00185 Roma, Italy
[48] INFN, Sezione di Roma 2, Università di Roma Tor Vergata, via della Ricerca Scientifica, 1 Roma, Italy
[49] INFN/National Institute for Nuclear Physics, via Valerio 2, 34127 Trieste, Italy
[50] IUCAA, Post Bag 4, Ganeshkhind, Pune University Campus, Pune 411 007, India
[51] Imperial College London, Astrophysics group, Blackett Laboratory, Prince Consort Road, London, SW7 2AZ, UK
[52] Infrared Processing and Analysis Center, California Institute of Technology, Pasadena, CA 91125, USA
[53] Institut d'Astrophysique Spatiale, CNRS (UMR 8617) Université Paris-Sud 11, Bâtiment 121, Orsay, France
[54] Institut d'Astrophysique de Paris, CNRS (UMR 7095), 98bis Boulevard Arago, 75014 Paris, France
[55] Institute of Astronomy, University of Cambridge, Madingley Road, Cambridge CB3 0HA, UK
[56] Institute of Theoretical Astrophysics, University of Oslo, Blindern, Oslo, Norway
[57] Instituto de Astrofísica de Canarias, C/Vía Láctea s/n, La Laguna, 38205 Tenerife, Spain
[58] Instituto de Física de Cantabria (CSIC-Universidad de Cantabria), Avda. de los Castros s/n, Santander, Spain
[59] Istituto Nazionale di Fisica Nucleare, Sezione di Padova, via Marzolo 8, 35131 Padova, Italy
[60] Jet Propulsion Laboratory, California Institute of Technology, 4800 Oak Grove Drive, Pasadena, California, USA
[61] Jodrell Bank Centre for Astrophysics, Alan Turing Building, School of Physics and Astronomy, The University of Manchester, Oxford Road, Manchester, M13 9PL, UK

[62] Kavli Institute for Cosmological Physics, University of Chicago, Chicago, IL 60637, USA
[63] Kavli Institute for Cosmology Cambridge, Madingley Road, Cambridge, CB3 0HA, UK
[64] Kazan Federal University, 18 Kremlyovskaya St., 420008 Kazan, Russia
[65] LAL, Université Paris-Sud, CNRS/IN2P3, 91400 Orsay, France
[66] LERMA, CNRS, Observatoire de Paris, 61 Avenue de l'Observatoire, 75014 Paris, France
[67] Laboratoire AIM, IRFU/Service d'Astrophysique – CEA/DSM – CNRS – Université Paris Diderot, Bât. 709, CEA-Saclay, 91191 Gif-sur-Yvette Cedex, France
[68] Laboratoire Traitement et Communication de l'Information, CNRS (UMR 5141) and Télécom ParisTech, 46 rue Barrault 75634 Paris Cedex 13, France
[69] Laboratoire de Physique Subatomique et Cosmologie, Université Grenoble-Alpes, CNRS/IN2P3, 53, rue des Martyrs, 38026 Grenoble Cedex, France
[70] Laboratoire de Physique Théorique, Université Paris-Sud 11 and CNRS, Bâtiment 210, 91405 Orsay, France
[71] Lawrence Berkeley National Laboratory, Berkeley, CA 94720 California, USA
[72] Lebedev Physical Institute of the Russian Academy of Sciences, Astro Space Centre, 84/32 Profsoyuznaya st., 117997 Moscow, GSP-7, Russia
[73] Max-Planck-Institut für Astrophysik, Karl-Schwarzschild-Str. 1, 85741 Garching, Germany
[74] McGill Physics, Ernest Rutherford Physics Building, McGill University, 3600 rue University, Montréal, QC, H3A 2T8, Canada
[75] National University of Ireland, Department of Experimental Physics, Maynooth, Co. Kildare, Ireland
[76] Nicolaus Copernicus Astronomical Center, Bartycka 18, 00-716 Warsaw, Poland
[77] Niels Bohr Institute, Blegdamsvej 17, 2100 Copenhagen, Denmark
[78] Optical Science Laboratory, University College London, Gower Street, WC1E 6BT London, UK
[79] SISSA, Astrophysics Sector, via Bonomea 265, 34136 Trieste, Italy
[80] School of Physics and Astronomy, Cardiff University, Queens Buildings, The Parade, Cardiff, CF24 3AA, UK
[81] Sorbonne Université-UPMC, UMR 7095, Institut d'Astrophysique de Paris, 98bis Boulevard Arago, 75014 Paris, France
[82] Space Sciences Laboratory, University of California, Berkeley, California, USA
[83] Special Astrophysical Observatory, Russian Academy of Sciences, Nizhnij Arkhyz, Zelenchukskiy region, 369167 Karachai-Cherkessian Republic, Russia
[84] Sub-Department of Astrophysics, University of Oxford, Keble Road, Oxford OX1 3RH, UK
[85] UPMC Univ Paris 06, UMR 7095, 98bis Boulevard Arago, 75014 Paris, France
[86] Université de Toulouse, UPS-OMP, IRAP, 31028 Toulouse Cedex 4, France
[87] University of Granada, Departamento de Física Teórica y del Cosmos, Facultad de Ciencias, 18071 Granada, Spain
[88] University of Granada, Instituto Carlos I de Física Teórica y Computacional, 18071 Granada, Spain
[89] Warsaw University Observatory, Aleje Ujazdowskie 4, 00-478 Warszawa, Poland

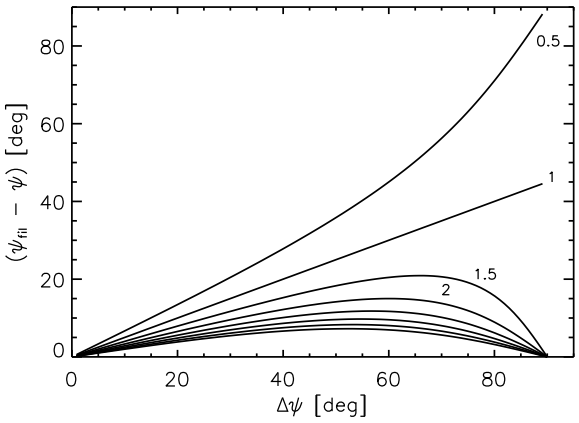

Fig. A.1. Difference between the intrinsic polarization angle of the filament, ψ_{fil}, and the observed polarization angle, ψ, as a function of $\Delta\psi = |\psi_{fil} - \psi_{bg}|$. The polarized intensity contrast of the filament is indicated close to the corresponding curves. It increases in steps of 0.5 from the top to the bottom curve. We note that for $\Delta\psi = 90°$ and $f_d = 1$, ψ is not defined and the resulting observed polarization fraction is null.

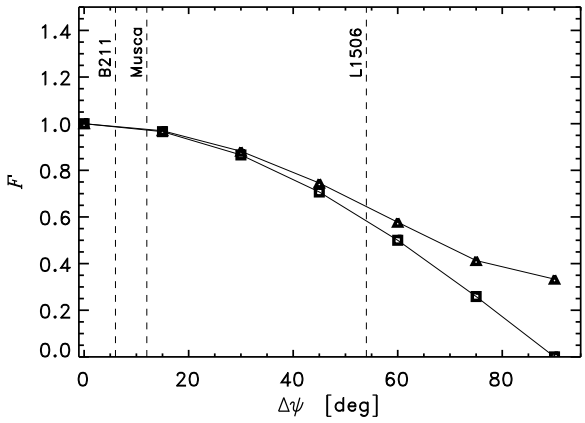

Fig. A.2. Depolarization factor due to the rotation of the field on the POS for two components with the same polarized intensity (squares) and with a contrast of two (triangles).

Appendix A: A two-component model along the LOS

The observed polarized emission results from the integration along the LOS of Stokes Q and U parameters of linearly polarized emission. Thus the observed polarization angle and fraction correspond to mean values of the emission along the LOS, which can be represented by the superposition of various layers/components with independent properties. A simplified two-component model applies as a first approximation to interstellar filaments and their backgrounds.

A.1. Mean polarization angle along the LOS

Here, we estimate the difference between the polarization angle ψ observed towards the filament, resulting from the integration of the emission along the LOS, and the intrinsic polarization angle of the filament ψ_{fil}. This difference depends on the polarized intensity contrast of the filament with respect to that of the background.

The observed Q and U emission integrated over the filament and the background are

$$Q = P_{bg}\,(f_d \cos 2\psi_{fil} + \cos 2\psi_{bg}), \quad (A.1)$$

$$U = P_{bg}\,(f_d \sin 2\psi_{fil} + \sin 2\psi_{bg}), \quad (A.2)$$

where P_{bg} is the polarized emission of the background, and $f_d = P_{fil}/P_{bg}$ the polarized intensity contrast between the two components. If the two components have the same polarized intensities ($f_d = 1$) the observed polarization angle ψ is equal to the average value, as can be seen in Fig. A.1. For $f_d > 1$, the difference between ψ_{fil} and ψ first increases with $|\psi_{fil} - \psi_{bg}|$ and then decreases when $|\psi_{fil} - \psi_{bg}|$ approaches 90°, while for $f_d < 1$, it increases with $|\psi_{fil} - \psi_{bg}|$. It is thus important to separate the components along the LOS, to access the underlying magnetic field orientation of the filament.

A.2. Depolarization from rotation of the POS component of the magnetic field

Here, we estimate the decrease in the polarized emission with respect to the total emission when two components with different field orientations overlap along the LOS.

For the simplified two-component model, the depolarization factor, F, can be expressed as

$$F = \frac{P}{P_{fil} + P_{bg}}, \quad (A.3)$$

where P is the observed polarized emission summed over the filament and the background. Equation (A.3) is equivalent to

$$F^2 = \frac{P^2}{P_{fil}^2 + P_{bg}^2 + 2P_{fil}P_{bg}}, \quad (A.4)$$

where $P^2 = U^2 + Q^2$ with $U = U_{fil} + U_{bg}$ and $Q = Q_{fil} + Q_{bg}$. Here Q and U are given by Eqs. (1) and (2) with the corresponding subscripts for the filament and the background. Thus

$$P^2 = P_{fil}^2 + P_{bg}^2 + 2P_{fil}P_{bg}\cos 2\Delta\psi, \quad (A.5)$$

where $\Delta\psi = |\psi_{fil} - \psi_{bg}|$. These relations lead to

$$F^2 = 1 - \frac{2P_{fil}P_{bg}(1 - \cos 2\Delta\psi)}{P_{fil}^2 + P_{bg}^2 + 2P_{fil}P_{bg}}, \quad (A.6)$$

which is equivalent to

$$F^2 = 1 - 2\frac{1 - \cos 2\Delta\psi}{(1 + f_d)^2} f_d, \quad (A.7)$$

with $f_d = P_{fil}/P_{bg}$. The maximal depolarization, i.e., the smallest value of F, equal to $|\cos\Delta\psi|$, is obtained for $P_{bg} = P_{fil}$.

The observed polarized emission of two components, due to the combination of the Stokes Q and U parameters along the LOS, results in depolarization if the POS magnetic field rotates in one component with respect to the other. P is zero if $\Delta\psi = 90°$ and the two components have the same polarized emission ($P_{fil} = P_{bg}$, see Fig. A.2). The depolarization factor towards the L1506 filament is $F \simeq 0.6$ for $\Delta\psi = 54°$ and a contrast of polarized emission of about one. For the Musca and B211 filament, F is close to unity since the POS angles in the filaments are close ($\Delta\psi \sim 10°$) to that of their backgrounds (cf. Table 2).